



2 **The importance of sequential partial melting and fractional
3 crystallization in the generation of syn-D₃ Variscan two-mica granites
4 from the Carrazeda de Ansiães area, northern Portugal**

5 R. J. S. Teixeira¹ · A. M. R. Neiva^{2,3} · M. E. P. Gomes¹ · F. Corfu⁴ · A. Cuesta⁵ · I. W. Croudace⁶

6 Received: 4 August 2020 / Accepted: 27 December 2020

7 © Universidad Complutense de Madrid 2021

8 **Abstract**

9 In the Carrazeda de Ansiães region, northern Portugal, a mesozonal granitic suite intruded Precambrian to Ordovician meta-
10 sedimentary rocks during the late kinematic stages of the Variscan orogeny. In this multiphase granitic complex, consisting of
11 ten granite types, the youngest group of two-mica granites (G7–G10) was emplaced between 318 ± 1 Ma and 316.2 ± 0.7 Ma,
12 as determined by ID-TIMS U–Pb on zircon and monazite. Granite types G7–G9 were affected by the third phase of defor-
13 mation (D₃) before they were completely crystallized, as indicated by their internal NW–SE magmatic foliation concordant
14 with the regional structures. The granite type G10 shows some distinctive textural features, showing a strong brittle defor-
15 mation, probably due to its preferential emplacement in late NNE–SSW fault zones. Granites G7–G9 have equal or higher
16 amounts of muscovite than biotite and contain surmicaceous enclaves, xenoliths, “schlieren”, and, more rarely, microgranular
17 enclaves. The muscovite-dominant granite G10 does not contain enclaves. These Variscan granites are peraluminous, with
18 ASI ranging between 1.22 and 1.39 and normative corundum of 2.79–4.39%, having the characteristics of S-type granites.
19 In fact, the enrichment in LREE relatively to HREE, the negative Eu anomalies, and similar mean values of ($^{87}\text{Sr}/^{86}\text{Sr}$)_i, ϵNd_t
20 and $\delta^{18}\text{O}$ for G7 (0.7156 ± 0.0005 ; –8.5; 11.49‰) and G8 (0.7155 ± 0.0007 ; –8.4; 11.39‰) show that these two granite
21 types resulted from sequential partial melting of the same metasedimentary material, where granite G8 would have derived
22 from a higher degree of partial melting than G7. Granites G8–G10 and their minerals show a fractionation trend that is
23 confirmed by modeling of major and trace elements. The subparallel REE patterns and the decreasing REE contents within
24 the differentiation series, the Rb–Sr isochron for G8, G9 and G10 (315.5 ± 5.4 Ma; MSWD = 1.3) and the relatively uniform
25 ϵNd_t and $\delta^{18}\text{O}$ data suggest that fractional crystallization was the main mechanism, which would have lasted less than 1 Ma.
26 The tin-bearing granites G7 and G10 have ≥ 20 ppm Sn, but the main quartz veins containing cassiterite and wolframite cut
27 granite G10, which contains 31 ppm Sn. Fractional crystallization was responsible for the increase in Sn content in granites
28 from the G8–G10 series and their micas.

29 **Keywords** S-type granites · U–Pb zircon and monazite ages · Isotopic data · Sequential partial melting · Fractional
30 crystallization · Tin

A1 A. M. R. Neiva: Deceased in 3rd May 2019.

A2 R. J. S. Teixeira
A3 rteixeir@utad.pt

A4 ¹ Department of Geology and Pole of the Geosciences Centre
A5 (CGeo), University of Trás-os-Montes e Alto Douro, UTAD,
A6 Quinta dos Prados, 5000-801 Vila Real, Portugal

A7 ² Department of Earth Sciences, University of Coimbra,
A8 3030-790 Coimbra, Portugal

A9 ³ GeoBioTec, Department of Geosciences, University
A10 of Aveiro, 3810-193 Aveiro, Portugal

4 Department of Geosciences and CEED, University of Oslo,
Blindern, PO Box 1047, 0316 Oslo, Norway

A11
A12

5 Department of Geology, University of Oviedo, C/ Jesús Arias
de Velasco s/n, 33005 Oviedo, Spain

A13
A14

6 Ocean and Earth Science, National Oceanography
Centre, University of Southampton, European Way,
Southampton SO14 3ZH, United Kingdom

A15
A16
A17

31 **Importancia de la fusión parcial secuencial y de la cristalización fraccionada en la formación
32 de granitos variscos sin-D₃ de dos micas en la región de Carrazeda de Ansiães, norte de
33 Portugal**

34 **Resumen**

35 En la región de Carrazeda de Ansiães, norte de Portugal, rocas metasedimentarias de edad Precámbrico y Ordovícico han
36 sido intruídas por una suite granítica mesozonal durante las etapas tardi-cinemáticas de la orogenia Varisca. En esta suite
37 se distinguen diez tipos de granitos en que los más jóvenes, constituidos por granitos de dos micas (G7–G10), se emplazan
38 entre 318 ± 1 Ma y 316.2 ± 0.7 Ma, de acuerdo con dataciones U–Pb ID-TIMS en circón y monacita. Los granitos G7–G9
39 han sido afectados por la tercera fase de deformación (D_3) antes de su consolidación completa, como sugiere su foliación
40 magmática interna NW–SE concordante con las estructuras regionales. El granito G10 tiene algunas características textur-
41 ales distintivas, propias de una fuerte deformación frágil, probablemente debidas a su emplazamiento preferente en zonas
42 de fallas tardías con dirección NNE–SSW. Los granitos G7–G9 tienen cantidades de moscovita iguales o mayores que las
43 de biotita y contienen enclaves “surmicaceous”, xenolitos, “schlieren” y, raras veces, enclaves microgranudos. El granito
44 G10 predominantemente moscovítico no contiene enclaves. Estos granitos variscos son peralumínicos, con valores de ASI
45 entre 1.22 y 1.39, y de corindón normativo entre 2.79–4.39%, y presentan características típicas de granitos de tipo S. De
46 hecho, el enriquecimiento en LREE con respecto a las HREE, las anomalías negativas de Eu y valores medios similares
47 de $(^{87}\text{Sr}/^{86}\text{Sr})_t$, ϵ_{Nd_t} y $\delta^{18}\text{O}$ para G7 (0.7156 ± 0.0005 ; –8.5; 11.49 %) y G8 (0.7155 ± 0.0007 ; –8.4; 11.39 %) muestran
48 que estos dos tipos de granito son el producto de la fusión parcial secuencial del mismo material metasedimentario, y que
49 el granito G8 correspondería a una mayor tasa de fusión parcial que el granito G7. Los granitos G8–G10 y sus minerales
50 muestran una evolución por fraccionación que se puede confirmar mediante la modelización de elementos mayores y traza.
51 Los espectros de REE subparalelos y la disminución de sus contenidos con la diferenciación, la isócrona Rb–Sr para G8, G9
52 y G10 (315.5 ± 5.4 Ma; MSWD = 1.3) y los valores relativamente uniformes de ϵ_{Nd_t} y $\delta^{18}\text{O}$ sugieren que la cristalización
53 fraccionada ha sido el principal mecanismo implicado, y habría tenido una duración inferior a 1 Ma. Los granitos espe-
54 cializados estanníferos G7 y G10 tienen contenidos de Sn ≥ 20 ppm, pero los principales filones de cuarzo con casiterita y
55 wolframita cortan al granito G10, que contiene 31 ppm de Sn. La cristalización fraccionada ha sido responsable del aumento
56 del contenido de Sn en los granitos de la serie G8–G10 y de sus micas.

57 **Palabras clave** Granitos de tipo S · Edades U–Pb en circón y monacita · Datos isotópicos · Fusión parcial secuencial ·
58 Cristalización fraccionada · Estaño

1 Introduction

Most granitoid plutons in the Central Iberian Zone of the Iberian Massif (Fig. 1a) were formed and emplaced during the last ductile regional Variscan deformation phase (D_3) (e.g., Ferreira et al., 1987; Azevedo and Nolan, 1998; Dias et al., 2002; Bea et al., 2003; Valle Aguado et al., 2005; Gutiérrez-Alonso et al., 2018). In the Carrazeda de Ansiães area, northern Portugal, this geological event is well marked by a suite of ten different S-type granite units, mainly derived by partial melting of metasedimentary rocks, followed by fractional crystallization or, more rarely, segregated from a sequential melting process (Teixeira, 2008). This paper reports the geology, mineralogy, petrology, geochemistry and isotopic compositions (Rb–Sr, Sm–Nd, $\delta^{18}\text{O}$) of the four youngest granite types of the granitic suite of Carrazeda de Ansiães, belonging to Group II (G7, G8 and G9) and Group III (G10) as defined by Teixeira (2008). The aim is to understand the processes responsible for their compositional variability and also the origin of high concentrations of tin in granites G7 and G10 and their micas. In

addition, this study also documents the challenging task of determining the crystallization ages of the four aforementioned granites by ID-TIMS U–Pb geochronology, in order to verify that they post-date the early syn- D_3 granites described by Teixeira et al. (2012b) in this area, as it is inferred by the geological field relations.

2 Geological setting

2.1 General features

The Carrazeda de Ansiães area (Northern Portugal) lies in the autochthonous segment of the Central Iberian Zone of the Iberian Massif that is dominated by a thick sequence of Precambrian to Lower Paleozoic metasediments deposited onto the ancient margin of Gondwana (Fig. 1; Pereira et al., 2018). Lower Ordovician volcanic/hypabyssal rocks also occur (e.g., Coke et al., 2011; Teixeira et al., 2013a, 2015). The metasedimentary sequence is known as Dúrico-Beirão Super Group and is subdivided in two groups: Douro Group

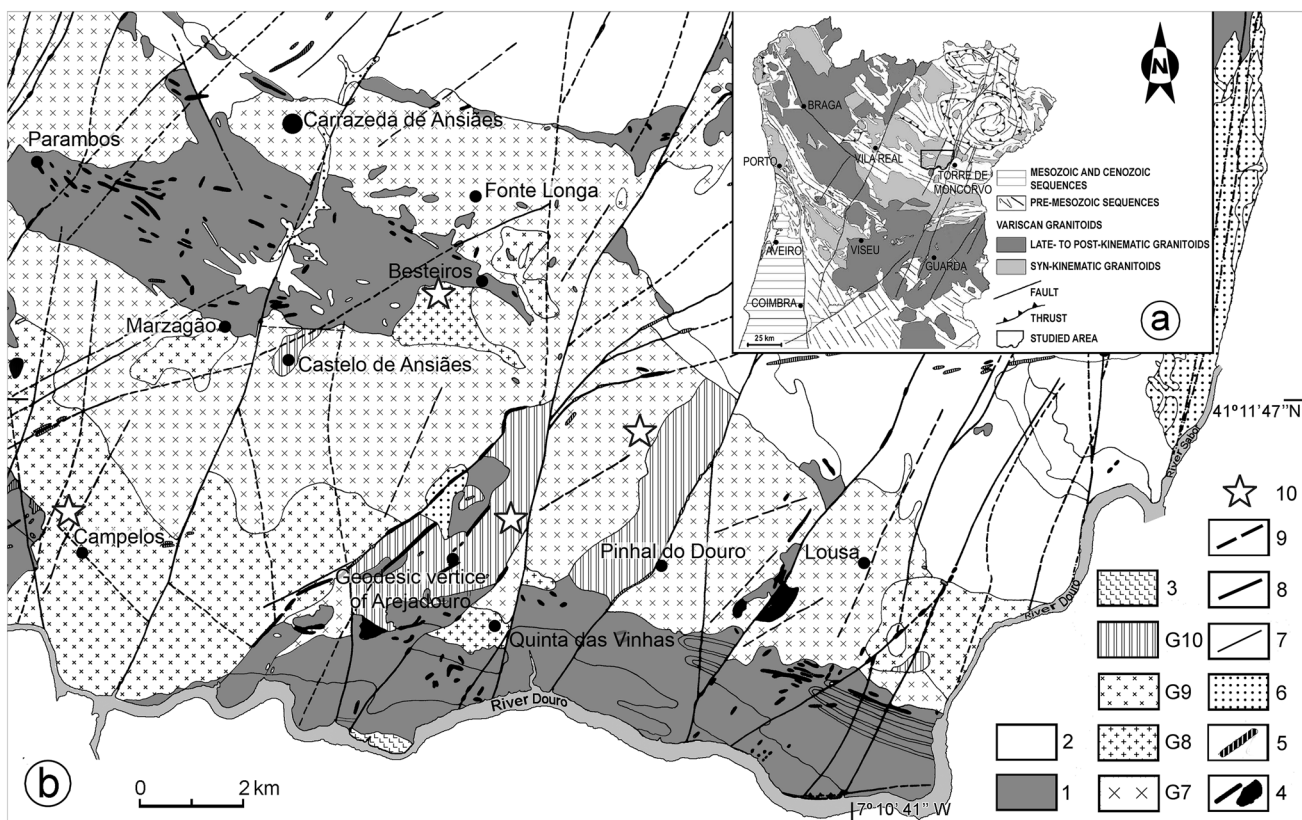


Fig. 1 a Distribution of Variscan syn- to post-kinematic granites from northern and central Portugal (Azevedo and Valle Aguado, 2006) and location of the Carrazeda de Ansiães area; b) Geological map of the area (after Silva et al., 1987/88). (1) metasedimentary formations of the Douro Group; (2) early syn-D₃ Variscan granites (Group I); G7—medium- to coarse-grained slightly porphyritic muscovite>biotite granite; G8—medium-grained porphyritic biotite ≈ muscovite granite;

G9—Medium-grained porphyritic muscovite>biotite granite; G10—Medium-grained slightly porphyritic muscovite-dominant granite; (3) late syn-D₃ Variscan granites; (4) rhyolitic porphyry, aplite, pegmatite and quartz veins; (5) lamprophyre and microgabbro; (6) sedimentary cover; (7) geological contact; (8) fault; (9) probable fault; (10) sampling sites for U-Pb dating

and Beiras Group (Oliveira et al., 1992). Large volumes of granitic rocks were emplaced in the Central Iberian Zone (CIZ) supracrustal rocks before, during and after the third phase of deformation of the Variscan orogeny (D₃), in a period constrained between ca. 347–337 Ma and ca. 290 Ma, as indicated by U-Pb data of zircon and monazite (e.g., Valle Aguado et al., 2005; Martins et al., 2009, 2013; Neiva et al., 2009; Teixeira et al., 2012b; Gutiérrez-Alonso et al., 2018).

The mesozonal intrusive granitic suite of Carrazeda de Ansiães intruded along the NW-trending core of the Vila Real—Torre de Moncorvo antiform formed during the D₁ and D₃ deformation phases (Silva et al., 1989; Fig. 1). This is in accordance with the typical spatial distribution of several groups of syn-D₃ granites in the Portuguese sector of the Central Iberian Zone, occurring along important NW–SE alignments that correspond either to the cores of D₃ antiforms or to transcurrent shear zones that would have accommodated the horizontal shortening produced in the final stages of the continental collision (Ferreira et al., 1987; Dias and Coke, 2006).

Based on field relationships and petrographic data it is possible to distinguish different types of granites in the Carrazeda de Ansiães area (Fig. 1b) that chronologically are arranged as follows: Group I, including granite types G1–G6; Group II, formed by granites G7–G9; and Group III, constituted only by granite G10.

Group I granites are anisotropic and show evidence of a magmatic foliation that was superposed by a more intense subparallel foliation formed in a ductile–brittle regime (Teixeira et al., 2012b). The internal structure of these granites (foliation) is concordant to those of the host metasedimentary rocks, showing a predominant NW–SE direction. The structural features suggest that granites of Group I would already have been consolidated (or at least in a submagmatic state) when they were affected by the third phase of deformation (D₃) (Teixeira et al., 2011, 2012b).

Group II granites were apparently deformed by D₃ before being completely crystallized, which explains the occurrence of an internal NW–SE magmatic foliation, concordant with the structure of host metasediments. This magmatic

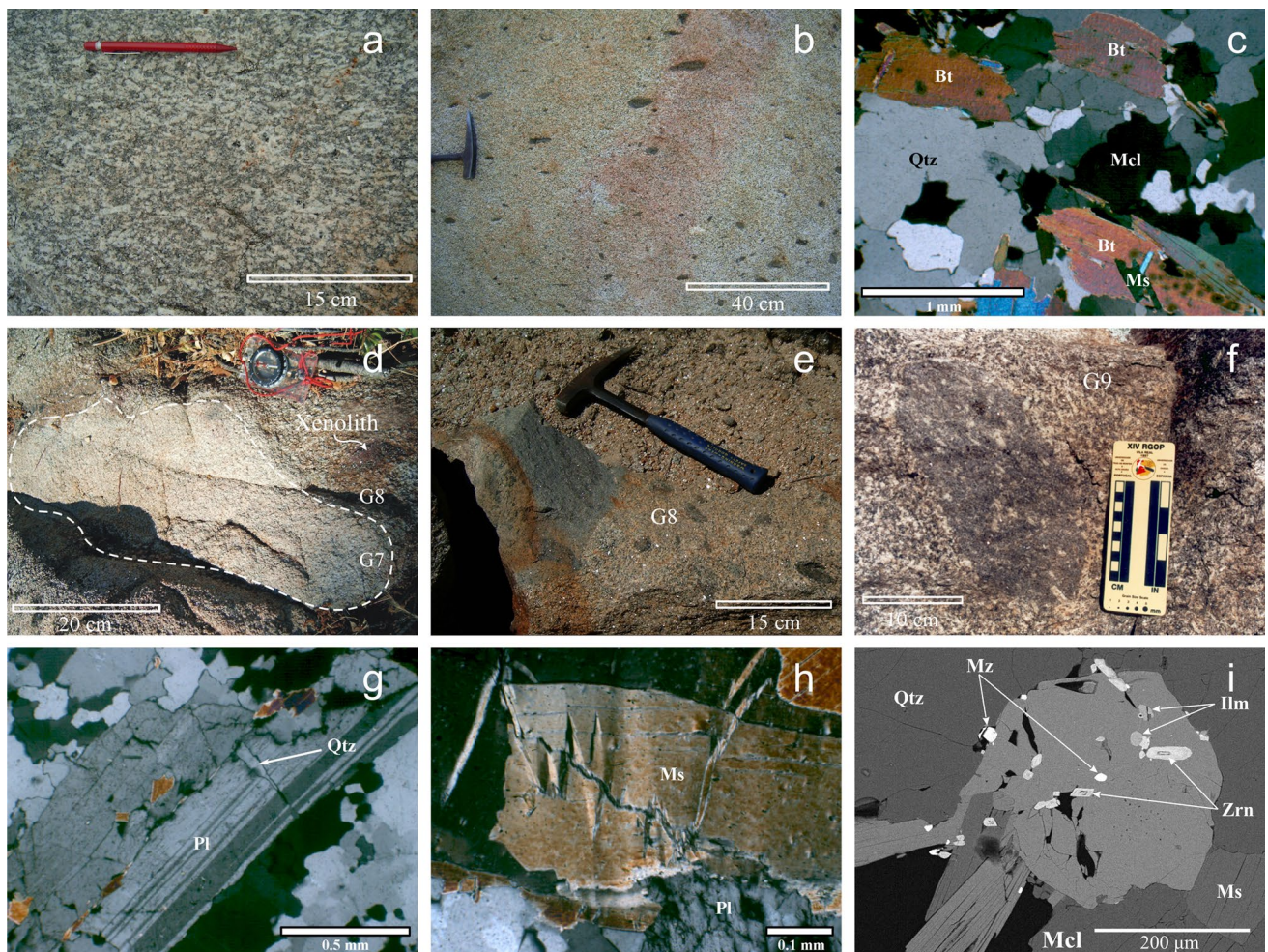


Fig. 2 **a** Magmatic foliation in granite G9 defined by feldspar phenocrysts; **b** Surmicaceous enclaves in granite G8, oriented parallel to the N55–60°W magmatic foliation; **c** Magmatic foliation in granite G8 defined by biotite. The quartz crystals of the matrix are only slightly deformed (photomicrograph in \times nicols); **d** Round-shaped enclave in granite G7 in granite G8; **e** Irregular-shaped tonalitic enclave in granite G8; **f** Fine-grained monzogranite enclave, partially enclosing phenocrysts of the host granite G9; **g** Microfracturing of plagioclase in

granite G10. One of the microfractures is filled with quartz (photomicrograph in \times nicols); **h** Muscovite from G10 granite affected by a microfracture and micro-scale “kink” type folding. The microfracture extends to the adjacent plagioclase crystal, subdividing into multiple branches (photomicrograph in \times nicols); **i** BSE image of an isolated crystal of apatite from granite G9, with inclusions of zircon, monazite and ilmenite. *Ap* apatite, *Bt* biotite, *Ilm* ilmenite, *Mcl* microcline, *Ms* muscovite, *Pl* plagioclase, *Qtz* quartz, *Zrn* zircon

foliation, more or less penetrative, is given by the orientation of feldspar phenocrysts, biotite (Fig. 2a), rarely by muscovite and, in the case of granite G8, by its abundant surmicaceous enclaves and xenoliths (Fig. 2b). The dominant magmatic nature of the structure of these granites is mainly recognized by the fact that the euhedral feldspar phenocrysts and the quartz crystals of the matrix are apparently undeformed (Fig. 2c). On the other hand, granite G10, belonging to Group III, shows textural features that suggest a faint overprint by D₃ during its emplacement, intimately associated to NNE-SSW fault zones, affected by N60–70° W and N40–50° E secondary joints (Sousa, 2000), and by strong brittle deformation (Teixeira, 2008; Fig. 1). However, locally there is evidence of a NW–SE magmatic foliation

concordant with the regional structure of host metasediments and defined by the orientation of feldspar phenocrysts and, sometimes, biotite. Thus, the geometry and localization of the different G10 granitic bodies (Fig. 1b) suggest that they were the youngest granite type of the region. The magmatic contacts between granites G8 (and G9) and granite G7 are always sharp, and, locally, the latter phase can occur in the form of rounded enclaves in granites G8 (Fig. 2d) and G9. There are no visible geological contacts between G8, G9 and G10. The geological contacts between granite G10 and G7, and to a lesser extent G9, are always defined by NNE-SSW faults (Fig. 1b).

According to the nomenclature of Didier and Barbin (1991), granites G7, G8 and G9 contain surmicaceous

150
151
152
153
154
155
156
157
158
159
160
161
162
163

enclaves, metasedimentary xenoliths and “schlieren” (Fig. 2b), and rare microgranular enclaves. In granite G8 there are irregular to rounded tonalitic enclaves that exhibit sharp contacts with the host granite (Fig. 2e), whereas granite G9 contains monzogranite enclaves that should correspond to fragments of early cold margins removed during magma ascent (Fig. 2f). The monzogranite enclaves partially enclose phenocrysts of the host granite G9 (Fig. 2f). Granite G10 does not contain enclaves.

3 Petrography

The most widespread rock type of Group II, G7, as well as G8 and G9, is monzogranite, whereas G10 of Group III is alkali feldspar granite since its plagioclase has less than 5% anorthite content (Le Maitre et al., 2002). These granites have a subhedral granular texture and contain microcline phenocrysts. Plagioclase phenocrysts are only observed in granite G8. They contain quartz, plagioclase, microperthitic microcline, biotite, some chlorite, muscovite, zircon, apatite, monazite, ilmenite, rutile and anatase (Table 1). Granites G7, G9 and G10 also have tourmaline, whereas sillimanite only occurs in granites G7, G8 and G9. Granite G8 has equal amounts of biotite and muscovite, G7, G9 and G10 are muscovite-dominant granites (Table 1).

Quartz is anhedral and contains inclusions of other minerals (e.g., acicular apatite, rutile, zircon and muscovite). In G10, quartz shows undulatory extinction and is intensely fractured (Fig. 2g).

Microcline is subhedral to anhedral in the matrix, but also forms subhedral microperthitic phenocrysts in all granites. It is cross-hatched twinned and contains inclusions of globular quartz, plagioclase, biotite, muscovite, zircon and apatite. Plagioclase is subhedral to anhedral and polysynthetically twinned. In general, the plagioclase grain boundaries are corroded by microcline, muscovite and quartz (Fig. 2g). Their fractures are filled by muscovite and quartz (Fig. 2g). Plagioclase phenocrysts only occur in G8 and have a composition of albite-oligoclase. Matrix plagioclase is albite-oligoclase in G7, G8 and G9 and albite in G10. Myrmekite occurs locally, while intensely fractured feldspars (Fig. 2g) and brecciated aggregates of plagioclase and microcline typically occur in G10.

Biotite and muscovite are commonly subhedral and intergrown, showing textures similar to those of primary muscovites of Miller et al. (1981) and Monier et al. (1984). However, some biotite grains are anhedral and corroded by feldspar and quartz. In the most deformed samples of G10, the micas show undulatory extinction, deformed cleavage planes and even some fracturing (Fig. 2h). Biotite is strongly pleochroic from β - and γ - reddish brown to α - yellow. Both

micas have inclusions of zircon, monazite, apatite (Fig. 2i) and ilmenite. Muscovite has rare inclusions of sillimanite.

Tourmaline is anhedral to subhedral and generally occurs as randomly or concentrically zoned crystals. It partially replaces plagioclase and micas, and usually contains inclusions of quartz, micas, feldspars, zircon and monazite. Tourmaline shows some fracturing, usually filled by quartz.

Zircon and monazite are euhedral and occur mainly included in biotite, muscovite and apatite (Fig. 2i), and locally in feldspars, quartz and tourmaline. Sillimanite occurs as needles in muscovite of G7, G8 and G9. Apatite is the most abundant accessory mineral (Fig. 2i), occurring included in micas, quartz and feldspars. Euhedral to subhedral ilmenite is included mainly in micas, zircon and apatite (Fig. 2i), whereas euhedral rutile is associated to ilmenite and monazite. Secondary muscovite replaces mainly plagioclase and biotite. Rare, secondary titanite and needle-shaped crystals of rutile are associated to minor chloritization of biotite.

4 Analytical methods

Samples were crushed in a jaw crusher and grinded in an agate mill. Major and trace elements were determined by X-ray fluorescence analysis at the National Oceanography Centre, University of Southampton, United Kingdom, using a Philips MagiX Pro PW 2540 wavelength dispersive XRF spectrometer fitted with a 4 kW Rh target X-ray tube and a VRC Sample Charger (Croudace and Thorpe, 1988; Croudace and Gilligan, 1990). Relative precision is $\pm 1\%$ for major elements and $\pm 5\%$ for trace elements.

The determination of whole rock FeO was carried out by titration with standardised potassium permanganate solution, whereas H₂O⁺ was determined with a Penfield tube, and Li by atomic absorption in the Laboratory of Chemistry of the University of Trás-os-Montes e Alto Douro, Vila Real, Portugal. The precision is $\pm 1\%$ for FeO and H₂O⁺ and $\pm 2\%$ for Li. Fluorine was determined by selective ion electrode analysis, with a precision of about 2%, at the SGS Laboratory, Canada (protocol ISE07A).

The REE¹ were determined by ICP-MS, with a precision of about 5%, at the SGS Laboratory, Toronto, Canada, following the protocol IMS95R.

Mineral analyses have been determined on an automated wavelength dispersive electron microprobe (Cameca Camebax SX-100) at the Scientific-Technical Services of

213
214
215
216
217
218
219
220
221
222
223
224
225
226
227
228
229
230
231

232

233
234
235
236
237
238
239
240
241

242
243
244
245
246
247
248
249
250
251
252
253

254
255
256

IFL01
IFL02
IFL03
IFL04
IFL05

¹ Main abbreviations used in this article: ICP-MS = Inductively Coupled Plasma Mass Spectrometry; L/M/H REE = Light/Middle/Heavy Rare Earth Elements; ID-TIMS = Isotope Dilution—Thermal Ionization Mass Spectrometry; XRF = X-Ray Fluorescence; MSWD = Mean Sum of Weighted Deviations.

Table 1 Geological, petrographic and geochemical characteristics of granites G7–G10 from Carrazeda de Ansiães area, northern Portugal

Granites/Location	Mineralogy	Texture and average dimensions for phenocrysts/Enclaves	Number, shape, size and deformation of the intrusions	Geochemical fingerprints	Source character and isotopes
<i>General features of granites G7–G10</i>	Quartz, plagioclase, micropo- rphyritic microcline, biotite, some chlorite, muscovite, tourmaline, zircon, apatite, monazite, ilmenite, rutile and anatase	Subhedral granular texture, containing feldspar phe- nocrysts	Peraluminous and alkali- calcic	Granites G7 and G8 are of S-type and result from the sequential partial melting of the same metasedimentary material	
<i>Granite G7</i> Along a WNW-ESE align- ment, from Parambos/Carr- azeda de Ansiães to Lousa	Muscovite > biotite granite Contains sillimanite	Medium- to coarse-grained slightly porphyritic granite; up to 2.5 × 0.9 cm Surmicaceous and meta- sedimentary xenoliths and “schlieren”	Crops out as a 81 km ² WNW-ESE trending body that intruded Douro Group metasediments and partially surrounds the early syn-D ₃ granites G3, G4, G5 and G6. A N50-60°W magmatic foliation is defined by biotite and more rarely by feldspar phenocrysts. This granite is affected by a NNE-SSW fracture system	ASI: 1.23–1.38 Normative corundum: 2.79–4.36% ΣREE: 101.1 ppm	Age: 317.8 ± 0.5 Ma $(^{87}\text{Sr}/^{86}\text{Sr})_i = 0.7156 \pm 0.0005$ $\varepsilon\text{Nd}_t = -8.5$ $\delta^{18}\text{O} = 11.35\text{--}11.62\text{‰}$
<i>Granite G8</i> Around and W of Quinta das Vinhais, and S of Besteiros, to the S and centre of the area, respectively	Biotite ≈ muscovite granite Contains sillimanite	Medium-grained porphyritic granite: from 1 × 0.4 cm to 2.4 × 0.8 cm Surmicaceous, metasedimen- tary xenoliths, monzogranite enclaves and granite G7 enclaves	Three distinct bodies, one of 1.5 km ² in the centre of the area with a WNW-ESE elongation, and two of 0.85 km ² and 0.25 km ² in the S. This homogeneous granite type intruded Douro Group metasediments and partially surrounds granite G7, show- ing sharp and fault contacts locally filled with aplite. It has a magmatic N55-60°W foliation defined by oriented feldspar phenocrysts, biotite and, locally, by surmicaceous enclaves and xenoliths	ASI: 1.22–1.39 Normative corundum: 2.85–4.39% ΣREE: 286.9 ppm	Age: 316.8 ± 1.3 Ma $(^{87}\text{Sr}/^{86}\text{Sr})_i = 0.7155 \pm 0.0007$ $\varepsilon\text{Nd}_t = -8.4$ $\delta^{18}\text{O} = 11.12\text{--}11.76\text{‰}$

Table 1 (continued)

Granites/Location	Mineralogy	Texture and average dimensions for phenocrysts/Enclaves	Number, shape, size and deformation of the intrusions	Geochemical fingerprints	Source character and isotopes
<i>Granite G9</i> Around Campelos and SW of Marzagão in the SW; SE of Fonte Longa in the centre and SE of Lousa in the SE of the area	Muscovite > biotite granite Contains sillimanite	Medium-grained porphyritic granite; from 2.5×0.7 cm to 0.9×0.3 cm Suriaceous and meta-sedimentary xenoliths, “schlieren”, G7 granite enclaves	A main body of 24 km^2 , with an approximated NW-SW elongation, and a smaller body of 1 km^2 in the SW. In the centre of the area there is another body of 1 km^2 , and a fourth body of 2.5 km^2 occurs to the SE of the area. This granite type intruded Douro Group metasediments and partially surrounds the early syn-D ₃ granites G3 and G5. This granite unit shows frequent sharp intrusive contacts with granite G7, but faulted contacts also occur. A N50-60°W magmatic foliation is defined by feldspar phenocrysts and biotite	ASI: 1.25–1.33 Normative corundum: 2.96–3.69% ΣREE : 189.1 ppm	Age: 316.6 ± 0.5 Ma $(^{87}\text{Sr}/^{86}\text{Sr})_i = 0.7151 \pm 0.0009$ $\varepsilon\text{Nd}_i = -8.3$ $\delta^{18}\text{O} = 11.10\text{--}11.33 \text{ ‰}$
<i>Granite G10</i> Around the geodesic vertice of Arejadouro and at NW of Pinhal do Douro in the S Around Castelo de Ansiães in the W	Muscovite-dominant granite	Medium-grained slightly porphyritic granite; (2×0.7 cm to 1×0.7 cm) Absence of enclaves	Three distinct homogeneous bodies, two of 4 km^2 and 6 km^2 in the S, and a third of 0.4 km^2 in the W, show a faint magmatic N60°W foliation defined by oriented feldspar phenocrysts and biotite. This granite intruded Douro Group metasediments and granite G7, and partially surrounds the early syn-D ₃ granite G4 and the granite G9, showing fault contacts. It occurs associated to NNE-SSW fault zones and it is affected by N60–70° W and N40–50° E secondary joints and strong brittle deformation.	ASI: 1.29–1.34 Normative corundum: 3.27–3.94% ΣREE : 64.2 ppm	Age: 316.2 ± 0.7 Ma $(^{87}\text{Sr}/^{86}\text{Sr})_i = 0.7147 \pm 0.0011$ $\varepsilon\text{Nd}_i = -8.4$ $\delta^{18}\text{O} = 10.93 \text{ ‰}$

257 the Department of Geology of University of Oviedo, Spain.
 258 The analyses were carried out with an accelerating voltage
 259 of 15 kV and a beam current of 15 nA. The precision is better
 260 than $\pm 2\%$ and the detection limits were generally $> 0.02\%$
 261 for most elements.

262 Trace element analyses of minerals were carried out on
 263 a VG Elemental Plasmaquad PQ2 + ICP-MS coupled to an
 264 ArF Excimer 4D Engineering laser system at the National
 265 Oceanography Centre, University of Southampton, United
 266 Kingdom (Gioncada et al., 2005). Measurements were
 267 performed using a 20 μm laser beam focused on polished
 268 250 μm thick sections. Following a pre-ablation period
 269 of 10 s, data were collected for 30 s. After collection, the
 270 data were corrected for instrumental drift and gas blank,
 271 and calibrated against the NIST 610 glass standard, where
 272 ten repeated measurements were reproducible to $\pm 7\%$. The
 273 detection limits were of 0.1–0.5 ppm.

274 The Sr and Nd isotope analyses were obtained at the
 275 Geochronology and Isotope Geochemistry-SGIker Facility
 276 of the Universidad del País Vasco UPV/EHU (Spain).
 277 Samples (0.050–0.200 g) were digested with $\text{HNO}_3 + \text{HF}$
 278 in PFA vials (Savillex) and in HF in high pressure PTFE
 279 bombs, employing the method of Pin and Santos Zaldegui
 280 (1997). The isotope ratios were then determined by thermal
 281 ionization mass spectrometry with a Finnigan MAT
 282 262. Normalization values were $^{86}\text{Sr}/^{88}\text{Sr} = 0.1194$ (Steiger
 283 and Jäger, 1977) and $^{146}\text{Nd}/^{144}\text{Nd} = 0.7219$ (Wasserburg
 284 et al., 1981). The values determined for the standards are
 285 $^{86}\text{Sr}/^{88}\text{Sr} = 0.710273 \pm 0.000018$ (2σ) for NBS 987, and $^{143}\text{Nd}/^{144}\text{Nd} = 0.511851 \pm 0.000045$ (2σ) for La Jolla. The ratios
 286 of $^{87}\text{Rb}/^{86}\text{Sr}$ were calculated from the concentrations of Rb
 287 and Sr determined by wavelength dispersive XRF, whereas
 288 the ratios of $^{147}\text{Sm}/^{144}\text{Nd}$ were calculated from the afore-
 289 mentioned ICP-MS data. Precision is $\pm 1\%$ for Rb and $\pm 5\%$
 290 for Sr, Sm and Nd.

291 Oxygen isotopic data of whole rock samples were deter-
 292 mined by gas mass spectrometry. The gas extraction was car-
 293 ried out at the Department of Earth Sciences, University of
 294 Western Ontario, Canada, employing chlorine trifluoride as
 295 the reagent (Clayton and Mayeda, 1963). A quartz standard
 296 was used and the precision was $\pm 0.2\text{‰}$.

297 Zircon and monazite were concentrated by a combina-
 298 tion of magnetic and heavy liquids separation procedures.
 299 Grains were subsequently selected by handpicking under a
 300 binocular microscope, and mechanically air abraded in order
 301 to remove external disturbed domains (Davis et al., 1982;
 302 Krogh, 1982). The U–Pb isotopic data for those minerals
 303 were obtained by ID-TIMS using a Finnigan MAT 262, at
 304 the Department of Geosciences, University of Oslo, Norway,
 305 following the standard methodology of Krogh (1973) with
 306 the adaptations described by Corfu and Evans (2002) and
 307 Corfu (2004). The decay constants are those from Jaffey
 308 et al. (1971) and the initial Pb correction was done using the

310 compositions calculated with the Stacey and Kramers (1975)
 311 model. The Isoplot program (Ludwig, 1999) was used for
 312 plots and regressions. All uncertainties of analyses are given
 313 at the 2σ level. Monazite mounting and their backscattered
 314 electron (BSE) imaging were carried out on the same elec-
 315 tron microprobe of University of Oviedo, Spain.

5 Whole rock geochemistry

316 The major and trace element contents of granites G7 to G10
 317 are given in Table 2. The aluminum-saturation index [Al/
 318 $(2(\text{Ca} - 1.67\text{P}) + \text{Na} + \text{K})$] from 1.22 to 1.39, and normative
 319 corundum range from 2.79 to 4.39%, show that all granites
 320 are peraluminous. Plotted in the diagrams of Frost and Frost
 321 (2008), these granites are magnesian and mainly belong to
 322 the alkali-calcic series.

323 Selected major and trace elements plotted against total
 324 Fe_2O_3 show two distinct regular trends, mainly defined by
 325 curves: (a) within the muscovite > biotite granite G7 samples
 326 (Fig. 3); (b) from the biotite \approx muscovite granite G8, musco-
 327 vite > biotite granite G9 to muscovite-dominant granite G10
 328 (Fig. 3a–c and Supplemental electronic Fig. 1). Total Fe_2O_3
 329 has been chosen as differentiation index because it shows
 330 more variability than SiO_2 .

331 The REE contents are low to moderate (64–287 ppm) and
 332 chondrite-normalized REE patterns are subparallel within
 333 the magmatic series G8–G9–G10 (Supplemental electronic
 334 data Table 1 and Fig. 4). From G8 to G9 and G10 there is a
 335 decrease in the ΣREE and in the enrichment in LREE with
 336 respect to HREE. The negative Eu anomaly also slightly
 337 increases from G8 to G9. The REE pattern of G7 follows
 338 a similar trend but it is characterized by a lower La_N/Lu_N
 339 average value (21.30) and a higher Eu/Eu^* value (0.37) than
 340 those from granites G8 (40.79 and 0.29, respectively) and
 341 G9 (36.21 and 0.27, respectively) (Supplemental electronic
 342 data Table 1).

343 The ocean-ridge granite-normalized diagram (Fig. 5)
 344 shows a general negative slope, with Rb, Th, Ce (except
 345 for G10) and Sm positive anomalies, Ba and Hf negative
 346 anomalies, and an enrichment in Rb and Th relatively to Nb.
 347 These features are characteristic of a crust dominant source
 348 (Pearce et al., 1984; Harris et al., 1986). The negative Ba
 349 and Hf anomalies suggest fractional crystallization of mainly
 350 K-feldspar and zircon.

6 Age and isotopic compositions

6.1 ID-TIMS U–Pb results on zircon and monazite

352 Granites G7–G10 have a diversified population of zircons,
 353 formed by autocrystic prisms but also by short to equant

Table 2 Average modal compositions and average whole-rock chemical analyses in wt.% and trace elements in ppm of granites G7–G10 from the Carrazeda de Ansiães area, northern Portugal

	G7	σ	G8	σ	G9	σ	G10	σ
Quartz	30.6	1.4	30.2	3.1	31.6	1.5	31.9	1.2
Plagioclase	31.6	2.5	27.8	2.1	29	1.6	32.4	1.8
Microcline	22.4	2	21.9	2	22.4	2.8	20.3	1.4
Biotite	5.1	0.5	9.7	2.1	6.1	0.5	2.3	0.3
Muscovite	9.8	1.8	9.7	2.2	10.3	1.1	12.5	1.1
Tourmaline	0.2	0.3	—	—	0.1	0.1	0.1	0.1
Apatite	0.4	0.1	0.5	0.1	0.4	0.1	0.6	0.2
Other	—	—	0.2	0.1	0.2	0.1	—	—
n	6		3		3		3	
SiO ₂	72.13	0.43	69.98	1.19	71.55	0.50	73.35	0.48
TiO ₂	0.21	0.04	0.45	0.07	0.31	0.02	0.13	0.02
Al ₂ O ₃	15.01	0.31	15.47	0.35	14.86	0.24	14.80	0.12
Fe ₂ O ₃	0.48	0.11	0.68	0.17	0.48	0.11	0.38	0.08
FeO	1.03	0.11	1.76	0.31	1.31	0.10	0.67	0.05
MnO	0.03	0.01	0.03	0.00	0.03	0.00	0.03	0.01
MgO	0.40	0.06	0.76	0.15	0.50	0.04	0.23	0.03
CaO	0.65	0.06	0.82	0.07	0.72	0.03	0.51	0.03
Na ₂ O	3.50	0.21	3.06	0.20	3.19	0.15	3.69	0.16
K ₂ O	5.05	0.18	5.44	0.18	5.23	0.20	4.66	0.21
P ₂ O ₅	0.33	0.03	0.35	0.01	0.33	0.02	0.34	0.02
H ₂ O +	0.84	0.22	0.98	0.07	1.07	0.06	1.01	0.07
H ₂ O –	0.33	0.10	0.30	0.04	0.30	0.05	0.26	0.07
S	0.01	0.01	0.01	0.00	0.01	0.00	0.01	0.00
Total	100.00	0.29	100.08	0.30	99.88	0.31	99.88	0.31
O ≡ S	0.01	0.01	0.00	0.00	0.00	0.00	0.00	0.00
Total	99.99	0.29	100.08	0.30	99.88	0.31	99.88	0.31
ASI	1.29	0.04	1.34	0.05	1.30	0.03	1.32	0.02
Corundum	3.40	0.43	3.89	0.52	3.43	0.25	3.60	0.21
Cl	110	0	56	9	50	0	60	10
F	1430	342	1955	78	2000	130	1673	345
Ga	21	2	24	0	23	1	22	1
Cr	34	8	38	3	40	6	32	3
V	8	2	23	6	13	1	5	1
Nb	14	2	13	1	12	1	16	1
Zn	67	16	91	10	87	7	62	6
Sn	20	3	10	2	15	2	31	4
Li	198	44	204	49	169	25	241	73
Ni	5	2	11	2	8	1	4	0
Co	3	1	7	1	5	1	3	1
Zr	73	30	201	29	140	12	53	7
Cu	4	2	10	3	5	2	5	4
Y	10	1	14	2	10	1	9	2
Sr	76	19	135	29	81	8	43	6
Pb	34	5	36	3	30	2	23	8
Ba	212	57	444	88	263	26	103	32
Rb	377	51	376	17	400	3	503	30
Cs	47	9	26	6	33	6	61	10
W	5	1	5	1	5	1	6	1
U	12	5	11	2	11	2	13	6
Th	12	6	35	4	26	2	7	3
Hf	*		5	1	4	0	*	

Table 2 (continued)

	G7	σ	G8	σ	G9	σ	G10	σ
As	5	1	8	0	5	2	4	0
Bi	2	0	*		*		2	0
n	17		8		10		8	

G7—Medium- to coarse-grained slightly porphyritic muscovite > biotite granite; G8—Medium-grained porphyritic biotite ≈ muscovite granite; G9—Medium-grained porphyritic muscovite > biotite granite; G10—Medium-grained slightly porphyritic muscovite-dominant granite; n—number of analyses; ASI— $Al/[2(Ca - 1.67P) + Na + K]$; σ —standard deviation; (—) not detected; *—below the limit of detection

356 crystals, which commonly contain visible cores. The
 357 autocrystic zircon crystals of granites G7–G10 are generally
 358 transparent, colourless to light brown and consist of euhedral
 359 prisms with terminal pyramid faces. These prisms can reach
 360 aspect ratios of up to >6:1, and commonly have melt inclusions.
 361 Monazite is euhedral to subhedral.

362 In granite G7, the two monazite analyses are reversely
 363 discordant (Fig. 6a), which is a common feature in this
 364 mineral due to the incorporation of significant amounts of
 365 ^{230}Th during its crystallization that leads to an excess of
 366 ^{206}Pb (Schärer, 1984; Corfu and Evins, 2002). Therefore,
 367 the weighted average $^{207}Pb/^{235}U$ age of fractions 6 and 7 of
 368 318 ± 1 Ma is considered the best indication of the crystal-
 369 lization age of granite G7. The five analysed zircon fractions
 370 from this sample are scattered. Two of them are younger
 371 than the monazites, probably due to some lead loss (frac-
 372 tions 4 and 5; Table 3 and Fig. 6a). The other three deviate
 373 towards older ages likely because of inherited components
 374 (fractions 1, 2 and 3; Table 3 and Fig. 6a).

375 Zircon fractions 10 and 11 from granite G8 yield a con-
 376 cordia age of 316.2 ± 0.8 Ma ($MSWD = 1.5$), whereas the
 377 only concordant monazite fraction 12 yields a $^{207}Pb/^{235}U$
 378 age of 317.4 ± 0.7 Ma (Table 3 and Fig. 6b). The combined
 379 age of 316.8 ± 1.3 Ma is considered the best indication for
 380 the crystallization age of this granite. The remaining zir-
 381 con fractions are discordant, showing lead loss (fraction 9;
 382 Fig. 6c) and an inherited component (fraction 8; Fig. 6c). A
 383 large amount of common lead in the monazite fraction 13
 384 (25 ppm; Table 3) significantly decreased the precision of
 385 the $^{207}Pb/^{235}U$ age (309.0 ± 7.9 Ma), which, however, still
 386 overlaps the combined zircon-monazite age. The mono-
 387 zite fraction 14 is reversely discordant yielding an older
 388 $^{207}Pb/^{235}U$ age of 334.4 ± 1.9 Ma, which could either be
 389 caused by uranium loss due to an alteration process (Poi-
 390 trasson et al., 1996; Corfu and Evins, 2002), as evidenced
 391 in Fig. 6d, or eventually to the presence of an inherited
 392 component.

393 Four multi-grain monazite analyses for granite G9 (frac-
 394 tions 19–22) show some dispersion (Table 3 and Fig. 6e),
 395 which is most probably explained by the presence of inher-
 396 ited components, as suggested by the BSE imaging of this
 397 mineral (Fig. 6f). Thus, the weighted average of $^{207}Pb/^{235}U$
 398 ages of the two youngest fractions (20 and 21) is considered

the best estimate for the crystallization of granite G9
 399 (316.6 ± 0.5 Ma). The four analysed zircon fractions are
 400 discordant, as they have inherited components.

401 Among the four analysed monazite fractions for granite
 402 G10, three are nearly concordant but show some dispersion
 403 in their $^{207}Pb/^{235}U$ ages (Table 3 and Fig. 6g). The BSE
 404 imaging also supports the existence of inherited components
 405 in some monazites of this granite, reason why the $^{207}Pb/^{235}U$
 406 age of the youngest fraction (29) is considered the most
 407 likely age of crystallization of granite G10 (316.2 ± 0.7 Ma).
 408 The remaining monazite fraction (28) is reversely discordant
 409 at an older $^{207}Pb/^{235}U$ age (341.1 ± 0.8 Ma). In the granite
 410 G10 none of the four zircon fractions is concordant (Fig. 6h),
 411 having been affected by lead loss (fractions 23 and 24;
 412 Table 3 and Fig. 6h) or by the presence of inherited compo-
 413 nents (fractions 25 and 26; Table 3 and Fig. 6h).

6.2 Whole rock Rb–Sr, Sm–Nd and oxygen isotope data

The Rb, Sr, Sm and Nd isotopic compositions of eleven whole rock samples were analysed (Supplemental elec-
 417 tronic data Table 2). The initial values calculated for
 418 an age of 317 Ma plot within a restricted domain from
 419 $(^{87}Sr/^{86}Sr)_i = 0.7133$ for G10 to 0.7161 for G7 and
 420 $\epsilon_{Nd_i} = -9.0$ to -7.6 for G9 (Fig. 7). Granitic rocks from
 421 the Carrazeda de Ansiães area partially match the isotopic
 422 composition of the Douro Group (Teixeira et al., 2012b) and
 423 northern CIZ metasediments (Villaseca et al. 1998, 2008,
 424 2014), although the hosting metasediments from the Douro
 425 Group tend to have somewhat more radiogenic Sr and less
 426 radiogenic Nd values, ranging from 0.7128 to 0.7188 and
 427 from -10.9 to -8.4 , respectively (Fig. 7). Granites G7 to
 428 G10 also plot near the isotopic fields established by Vil-
 429 laseca et al. (1999) for lower crust felsic granulites and
 430 orthogneisses from the Spanish Central System. The mean
 431 T_{DM} ages range from 1.28 Ga to 1.86 Ga (Supplemental
 432 electronic data Table 2), which are typical values for Vari-
 433 scan granites (e.g., Liew and Hofmann, 1988; Dias et al.,
 434 2002).

Three samples of G8, three samples of G9 and two sam-
 435 ples of G10 define a Rb–Sr whole rock isochron yielding
 436 an age of 315.5 ± 5.4 Ma and $(^{87}Sr/^{86}Sr)_i = 0.7155 \pm 0.0010$

(MSWD = 1.3; Fig. 8). This Rb–Sr age overlaps the more precise ages obtained by U–Pb in zircon and monazite.

The mean oxygen isotopic compositions of eight representative samples of granites G7 to G10 range from 10.93 to 11.49 ‰ (Supplemental electronic data Table 2). Such high $\delta^{18}\text{O}$ values are typical of Variscan granitic rocks in Europe (e.g., Hoefs and Emmermann, 1983; Neiva and Gomes, 2001), which have been explained by anatexis of metasedimentary sources (Hoefs, 2009).

7 Geochemistry of minerals

7.1 Feldspars

The compositions of microcline and plagioclase are given in Supplemental electronic data Table 3. The orthoclase contents in phenocryst and matrix microcline of granites G7 to G10 are similar (89–98 mol %; Supplemental electronic data Table 3), but the BaO content decreases from phenocryst to matrix in all studied granites, suggesting a magmatic origin of this mineral (e.g., Nekvasil, 1992). The BaO content in phenocryst microcline is identical in granites G7 and G8 and is higher in the matrix of G8 than in that of G7. Furthermore, the BaO content of microcline decreases from G8 to G9 and G10 (Supplemental electronic data Table 3). Some trace elements of matrix microcline plotted versus whole rock total Fe_2O_3 define a trend from G8 to G10 (Supplemental electronic data Table 3 and Supplemental electronic Fig. 2a). The data for microcline from G7 plot outside this trend (Supplemental electronic Fig. 2a).

Plagioclase from granites G7 to G10 is normally zoned, with the anorthite content decreasing from core to rim, and from phenocryst to matrix in G8. The anorthite content of matrix plagioclase from G8 is higher than that from G7, and decreases from G8 to G9 and G10 (Supplemental electronic data Table 3). Some major and trace elements of matrix plagioclase, plotted versus whole rock total Fe_2O_3 , define curvilinear trends from G8 to G9 and G10 (Supplemental electronic data Table 3 and Supplemental electronic Fig. 2b). The data for plagioclase from G7 do not fit these trends (Supplemental electronic Fig. 2b).

Although the P_2O_5 content of both feldspars is ≤ 0.58 wt.% in granites G7 to G10 (Supplemental electronic data Table 3), there is a general increase in P_2O_5 from microcline and plagioclase of G8 to those of G9 and G10 (Supplemental electronic data Table 3). The microcline contains more P_2O_5 than coexisting plagioclase, which is in accordance with findings by London et al. (1990), Neiva (1998) and Antunes et al. (2008). The empirical distribution coefficient D[P]Kf/Pl between K-feldspar and plagioclase ranges from 1.38 and 3.00. This coefficient should be about 1.2 in natural feldspars, close to their orthoclase and albite end members,

when in equilibrium (London et al., 1999). Granite G10 has D[P]Kf/Pl = 3.00 indicating that its microcline started to crystallize before albite or, eventually, that albite was formed from a magma already depleted in phosphorous.

7.2 Micas

The average compositions of biotite and muscovite are given in Supplemental electronic data Table 4. Biotites have $\text{Mg}/(\text{Mg} + \text{Fe}^{2+} + \text{Fe}^{3+})$ ranging from 0.16 to 0.36 (Rieder et al., 1999) and compositions similar to those found in biotites from aluminium-potassic rock series of the biotite ± cordierite and biotite ± muscovite fields (Nachit et al., 1985). The biotites from G8 to G10 define fractionation trends for major and trace elements. In general, the data for biotite from G7 do not fit those trends (Supplemental electronic Fig. 3a).

Muscovites from G7 to G10 have high TiO_2 and Al_2O_3 and low MgO contents (Supplemental electronic data Table 4) and so are magmatic (Miller et al., 1981; Monier et al., 1984). Variation diagrams for major and trace elements of muscovite versus whole rock total Fe_2O_3 show a trend from G8 to G10 but do not include G7 (Supplemental electronic Fig. 3b).

7.3 Ilmenite

Ilmenite occurs in all granites and its mean Mn content ranges from 0.137 to 0.274 pfu (Supplemental electronic data Table 5). Negative correlations were found between Mn and Fe^{2+} , and between Ti and $\text{Fe}^{2+} + \text{Fe}^{3+} + \text{Mn}$ of ilmenite from granites G7 to G10. Mn and $\text{Mn}/(\text{Mn} + \text{Fe}^{2+})$ increase and Fe^{2+} decreases from the ilmenite of G8 to the ilmenite of G9 and G10 (Supplemental electronic Fig. 3c).

8 Regional correlation

The majority of granitic rocks from the Central Iberian Zone were emplaced at upper and middle crustal levels during the deformation phase (D_3), following the crustal thickening and subsequent extension related to the Variscan continent–continent collision (Gutiérrez-Alonso et al., 2018). Therefore, the granitic rocks from northern and central Portugal have been classified according to their relation with the aforementioned deformation phase as: syn-orogenic pre- D_3 , syn- D_3 (~320–310 Ma) and late- D_3 (310–300 Ma), and late- to post orogenic (post- D_3) (~296–290 Ma) (Dias et al., 1998; Ferreira et al., 1987; Valle Aguado et al., 2005). The U–Pb geochronological data for the studied granites, together with the geological field relations, may be interpreted as reflecting two generations of syn- D_3 granites: (1) the oldest is granite G7 formed at 318 ± 1 Ma; (2) the youngest, formed in the interval of 316.8 ± 1.3 Ma and 316.2 ± 0.7 Ma, includes

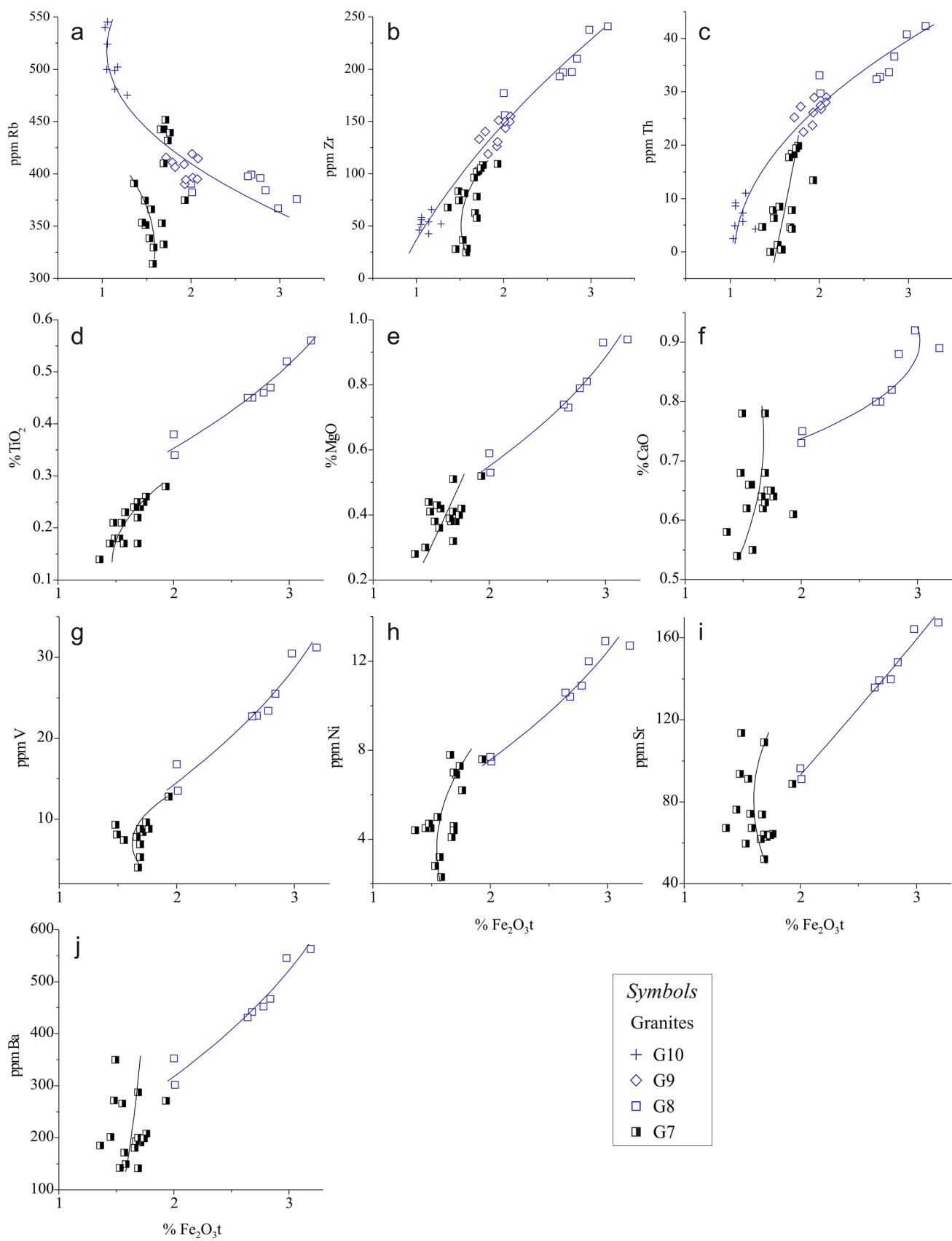


Fig. 3 Variation diagrams for whole rock major and trace element concentrations in granites G7–G10 from Carrazeda de Ansiães area. The samples of granite G7 define one trend, whereas granites G8, G9 and G10 define a different trend. The samples richest in Rb of granite G7 reflect some metasomatic effects and, therefore, were not considered in the curvilinear regression

535 granites G8–G10. The compositions of these granites project
536 in the field of syn-collision granites in the R_1 – R_2 diagram
537 (La Roche et al., 1980; Batchelor and Bowden, 1985) and
538 also in the tectonic discrimination diagrams of Pearce et al.
539 (1984).

540 9 Petrogenesis

541 9.1 Anatetic granitic rocks and their protoliths

542 Major and trace elements variations suggest that the musco-
543 vite > biotite granite G7 and the biotite ≈ muscovite granite
544 G8 formed during distinct magmatic pulses (Fig. 3a–c). Evi-
545 dence includes the REE patterns, with a distinct enrichment
546 in the LREE (Fig. 4), trace and major elements in micro-
547 cline (Supplemental electronic Fig. 2a), plagioclase (Supple-
548 mental electronic Fig. 2b), biotite (Supplemental electronic
549 Fig. 3a) and muscovite (Supplemental electronic Fig. 3b),
550 but also the existence of intrusive and sharp contacts
551 between granites G8 (and G9) and the granite G7, whereas
552 those between granite G10 and G7 and, to a lesser extent,
553 G9, are always associated to NNE-SSW faults. There are no
554 visible intrusive contacts between G8, G9 and G10 (Fig. 1).

555 Granites G7 and G8 are peraluminous, with ASI ranging
556 from 1.22 to 1.39 (Table 1), and hence contain aluminum-
557 rich minerals such as biotite, muscovite and sillimanite.
558 These granites also have ilmenite, $K_2O > Na_2O$, low CaO/Na_2O ,
559 an enrichment in LREE relative to HREE, negative
560 Eu anomalies, $(^{87}Sr/^{86}Sr)_i = 0.7136$ to 0.7160, $\epsilon Nd_t = -9.0$
561 to -7.6 and $\delta^{18}O = 10.93\text{--}11.49 \text{‰}$ (Supplemental elec-
562 tronic data Table 2), highlighting their affinity to S-type
563 magmas (Chappell and White, 1992). Taking into account
564 that metapelitic rocks have $CaO/Na_2O < 0.5$, in con-
565 trast to metagreywacke or meta-igneous rocks with $CaO/Na_2O = 0.3\text{--}1.5$, Jung and Pfänder (2007) used this ratio
566 to infer the source composition of peraluminous granites.
567 In granites G7 and G8 the CaO/Na_2O ratios are 0.18 and
568 0.27, respectively, which supports an origin from a mainly
569 metapelitic source. Furthermore, the similarity in the mean
570 $(^{87}Sr/^{86}Sr)_i$ and ϵNd_t values of granites G7 and G8 also indi-
571 cate that these magmas were formed by partial melting of
572 a common metapelitic source with a composition compara-
573 ble to those of Douro Group and northern CIZ metasedi-
574 ments (Villaseca et al., 1998, 2008, 2014; Teixeira et al.,
575 2012b). The U–Pb ID-TIMS data allow to infer that granites

577 G7 and G8 contain Neoproterozoic inherited zircon compo-
578 nents (cores, most likely) with ages comparable to those of
579 detrital zircons in metasediments of the Douro Group (e.g.,
580 Teixeira et al., 2012a, 2013b), thus supporting their involve-
581 ment in the origin of the granitic magmas. A fairly identical
582 model involving the partial melting of Neoproterozoic to
583 lower Palaeozoic supracrustal rocks has also been proposed
584 to explain the origin the Variscan granites in the Eastern
585 Erzgebirge/Krušné hory, Central Europe (e.g., Förster and
586 Romer, 2010; Romer et al., 2011; Breiter, 2012). However, it
587 should be reminded that the isotopic composition of granitic
588 magmas derived from a source at depth does not necessarily
589 have a one-to-one relationship, particularly concerning Sr,
590 to the equivalent metamorphic rocks at the level of granitic
591 emplacement. In fact, Miller et al. (1992) and Villaseca et al.
592 (1999) argue that, in orogenic areas, granite sources are not
593 the outcropping metamorphic rocks, but those located at
594 deeper crustal levels.

595 Although the geochemical and isotopic signatures of
596 granites G7 and G8 indicate a major role of a supracrustal
597 protolith in the genesis of these magmas, the granite G8 of
598 the Carrazeda de Ansiães area also contains some tonalitic
599 enclaves, which may point to a local interaction between
600 felsic crustal melts and mafic to intermediate mantle-derived
601 magmas, enough to generate somewhat more primitive iso-
602 topic signatures, as for instance in sample GQV9 of gran-
603 ite G8. This mechanism has also been invoked to explain
604 the origin of Variscan granitic intrusions elsewhere in the
605 Central Iberian Zone (e.g., Costa et al., 2014; Gomes et al.,
606 2014) and in the French Massif Central (e.g., Williamson
607 et al., 1996; Ledru et al., 2001), as well as to explain the
608 whole range of compositions and geochemical trends of
609 granites of the Peninsula pluton, South Africa (Garcia-Arias
610 and Stevens, 2017).

611 9.2 Sequential partial melting of G7 and G8

612 Granite G7 has a lower biotite/muscovite proportion (0.5)
613 than G8 (1.0). From G7 to G8 there is an increase in Zr, Th,
614 TiO_2 , MgO , CaO , V, Ni, Sr and Ba with increasing Fe_2O_3
615 (Fig. 3b–j), indicating that granite G8 could result from a
616 higher degree of partial melting than granite G7 (Holtz and
617 Barbey, 1991). Furthermore, granite G7 shows geochemical
618 trends in the variation diagrams (Fig. 3) that seem to con-
619 tinue into G8, suggesting a relation between both granites.
620 However, a fractional crystallization process is not adequate
621 to explain their genesis because G7 is the most evolved and
622 was emplaced up to ~ 1 Ma earlier than granite G8. These
623 two granites have identical Rb, $(^{87}Sr/^{86}Sr)_i$, ϵNd_t and $\delta^{18}O$
624 values and subparallel REE patterns, but granite G8 is richer
625 in ΣREE and has higher La_N/Lu_N average values than G7
626 (Fig. 4). Both granites also contain surmicaceous enclaves
627 but these are much more abundant in granite G8, which is

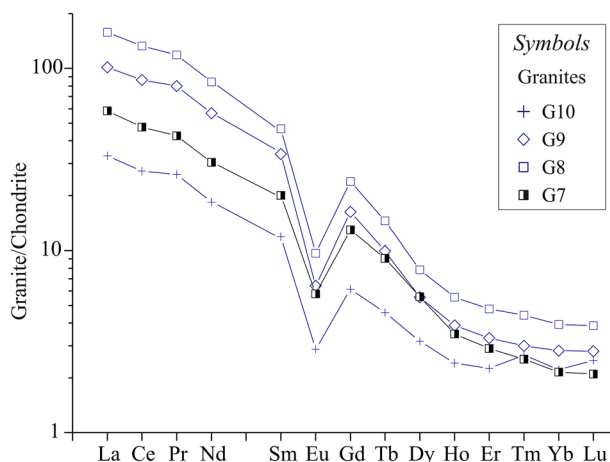


Fig. 4 Average chondrite-normalized REE abundances for granites G7–G10 from Carrazeda de Ansiães area, northern Portugal. Chondrite abundances from Taylor and McLennan (1985)

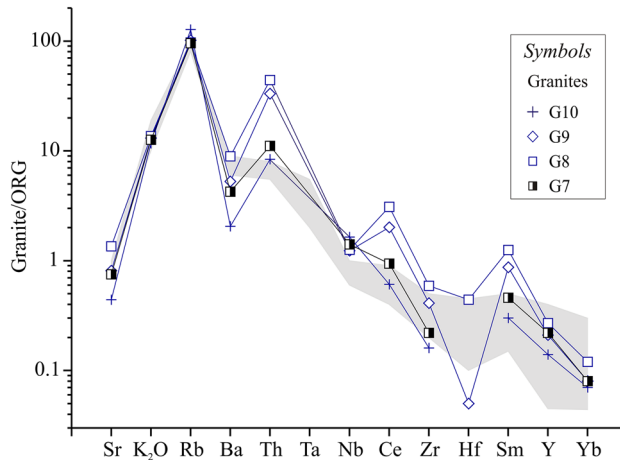


Fig. 5 Ocean-ridge granite-normalized (ORG) diagram of Pearce et al. (1984) and Harris et al. (1986) for granites G7–G10 from Carrazeda de Ansiães area, northern Portugal. The shaded area corresponds to syn-collisional granites from Harris et al. (1986)

628 compatible with a higher degree of partial melting (Holtz
629 and Barbey, 1991; Teixeira, 2008).

630 An estimate of the temperature of formation of unfrac-
631 tionated granitic magmas can be obtained from the Al₂O₃/
632 TiO₂ ratio, since magmas with low ratios are generated at
633 higher temperatures than those with high Al₂O₃/TiO₂ ratios
634 (Sylvester, 1998; Jung and Pfänder, 2007). On this basis,
635 granite G8 (Al₂O₃/TiO₂=34.74) originated at a higher tem-
636 perature than G7 (Al₂O₃/TiO₂=72.53). The conditions of
637 formation of granitic magmas can also be obtained from
638 the zircon saturation equation (Watson and Harrison, 1983),
639 assuming equilibrium conditions. The average zircon sat-
640 uration temperature (Tzr) is of 816 °C for G8 and 734 °C

for G7, which indicates a higher degree of partial melting
641 for G8 (Miller et al., 2003). However, these Tzr values are
642 overestimated since there are inherited zircon cores in both
643 granites (Watson and Harrison, 1983).

644 Matrix microcline from G8 has a higher Ba content than
645 the corresponding microcline in G7 (Supplemental elec-
646 tronic data Table 3), while anorthite content of matrix plati-
647 oclase from G8 is higher than that from G7 (Supplemental
648 electronic data Table 3). Both phenocryst- and matrix-feld-
649 spars from G8 have less P₂O₅ than those in G7 (Supple-
650 mental electronic data Table 3). Biotite and muscovite from G8
651 have more MgO and less Li than those from G7 (Supple-
652 mental electronic data Table 4), whereas muscovite from G7
653 is richer in F than that from G8 (Supplemental electronic data
654 Table 4). Therefore, the mineral compositions support that
655 G8 was formed at a higher temperature than G7 and also
656 confirm that they are not related by a fractional crystallization
657 mechanism.

658 The apparently sequential partial melting evolution from
659 muscovite > biotite granite G7 (318 ± 1 Ma) to biotite ~ mus-
660 covite granite G8 (316.8 ± 1.3 Ma) from the Carrazeda de
661 Ansiães area is comparable to that observed for other Portu-
662 guese Variscan granites, namely those from the Tourém area
663 (Holtz and Barbey, 1991; Neiva, 1994), the Guarda-Sabugal
664 area (Neiva et al., 2011a) and the Penafiel area (Carvalho
665 et al., 2012), and also in other areas elsewhere, e.g., those in
666 the Achiras complex, Córdoba, Argentina (Otamendi et al.,
667 1998).

668 The generation of granitic rocks from the same source
669 by sequential partial melting is a rare process, whose occur-
670 rence in Portugal is mainly explained by the combination of
671 an intense crustal thickening during the Variscan orogeny
672 that established a high geothermal gradient, and the subse-
673 quent collapse, extension and mantle upwelling (Clemens,
674 2003; Valle Aguado et al., 2005; Gutiérrez-Alonso et al.,
675 2018). At Carrazeda de Ansiães area, this is also supported
676 by the presence of scarce tonalitic enclaves in granite G8,
677 formed at higher temperatures, and their absence in granite
678 G7.

9.3 Series of fractional crystallization

680 Granites G8, G9 and G10, with identical crystallization
681 ages, at 316.8 ± 1.3 Ma, 316.6 ± 0.5 Ma and 316.2 ± 0.7 Ma,
682 respectively, but with no visible intrusive contacts, seem
683 to define a magmatic differentiation series as they define
684 curvilinear trends in major and trace elements diagrams
685 (Fig. 3a–c and Supplemental electronic Fig. 1), and show
686 decreasing Ba contents of phenocryst and matrix microcline
687 (Supplemental electronic data Table 3), decreasing anor-
688 thite content of plagioclase (Supplemental electronic data
689 Table 3), fractionation trends for microcline (Supplemental
690 electronic Fig. 2a), plagioclase (Supplemental electronic
691

Fig. 2b), biotite (Supplemental electronic Fig. 3a), muscovite (Supplemental electronic Fig. 3b) and ilmenite (Supplemental electronic Fig. 3c), and subparallel whole rock REE patterns within each series (Fig. 4). The decrease in LREE from G8, to G9 and G10 can be explained by fractionation of monazite (Bea, 1996), whereas the decrease in the MREE can be due to apatite fractionation (Henderson, 1984), and the decrease in HREE to zircon fractionation (Yurimoto et al., 1990; Bea, 1996), in agreement with the decrease in Zr from G8 to G9 and G10 (Table 2). The Sr and Nd isotopic compositions are relatively uniform, although with some differences in G8, G9 and G10 and even within each granite type (Fig. 7). There is no significant variation in $\delta^{18}\text{O}$ values, which also supports a fractional crystallization mechanism. The slightly decrease in the $\delta^{18}\text{O}$ value of granite G10 can be attributed to some oxygen-isotope exchange at subsolidus temperature between feldspar and quartz (Blattner et al., 2002). Furthermore, $(^{87}\text{Sr}/^{86}\text{Sr})_l$ versus $1/\text{Sr}$ does not define a positive correlation for the series, which would confirm that assimilation or mixing processes did not play a major role.

Major and trace element contents were used for testing fractional crystallization. The average of the two least silicic samples of granite G8 was selected as the starting magma, while the average of the two most silicic samples of G8, the average of samples GC8 and GC7 of granite G9 and three samples of G10 (GAJ13, GAJ8 and GAJ11), free of metasomatic effects, were selected as residual liquids. The least-squares regression method was applied to model major elements using pure anorthite, albite, K-feldspar and quartz compositions together with the compositions of biotite and ilmenite analysed with the electron microprobe in the G8 sample with the lowest SiO_2 content. The calculated compositions of parent magma for the granites compare well with the respective determined parent granite and the sum of the squares of the residuals ΣR^2 is ≤ 0.0115 (Supplemental electronic data Table 6). The anorthite content of fractionating plagioclase in the cumulate is close to that of the core of plagioclase phenocrysts in the G8 sample with the lowest SiO_2 . The percentages of quartz and K-feldspar increase and those of plagioclase, biotite and ilmenite decrease in the cumulate versus the decrease in the weight fraction of melt remaining during fractional crystallization (Supplemental electronic data Table 6). The perfect (or Rayleigh) fractional crystallization equation, the modal compositions of cumulate and weight fraction of melt remaining during fractional crystallization, based on calculations involving major elements and the distribution coefficients of Arth (1976) and Nash and Crecraft (1985), were used for modelling Sr, Ba and Rb, which are the most informative trace elements for evaluating the fractionation of granitic rocks. Strontium and Ba decrease and Rb increases with the decrease in the remaining melt during fractional crystallization from G8 to G9 and G10 (Supplemental electronic data Table 6). The calculated

Sr, Ba and Rb values are consistent with the measured data although the calculated Sr and Ba values for G10 are generally higher and the calculated Rb, Rb/Ba and Rb/Sr ratios are lower than the measured data (Supplemental electronic data Table 6 and Supplemental electronic Fig. 4). This may be due to uncertainties in the distribution coefficients and the possibility that magmatic fluids might have controlled the behaviour of LIL elements in the most evolved granitic rocks (e.g., Neiva 1998; Antunes et al., 2008; Huang et al., 2014; Xu et al., 2015; Romer and Kroner, 2016; Pan et al., 2018; Roda-Robles et al., 2018; Nguyen et al., 2019).

The described process is in agreement with the studies done on other European Variscan granitic plutons where fractional crystallization contributed to an enrichment in lithophile and fluxing elements, namely in granites of the Cornubian batholith, England (Müller et al., 2006; Simons et al., 2016, 2017; Smith et al., 2019), in some granites of Krušné hory/Erzgebirge Mountains, Central Europe (Breiter, 2012), in the highly evolved peraluminous granite of Belvís de Monroy, Spain (Merino Martínez et al., 2014), but also in granitic suites elsewhere, e.g., along the southeastern margin of the North China Craton (Li et al., 2020), in the Mufushan complex, South China (Wang et al., 2014) and in the Lhasa Terrane, southern Tibet (Zhang et al., 2019).

10 Tin content of granites and its origin

Among the late syn-D₃ granitic suite of Carrazeda de Ansiães (G7–G10), the only Sn-bearing granites in the sense of Neiva (1984) and Lehmann (1990) are the muscovite > biotite granite G7 and muscovite-dominant granite G10, with mean Sn contents of 20 and 31 ppm, respectively (Table 2). The main occurrences of tin- and tungsten-bearing quartz veins are in granite G10, but some are also spatially related with G7.

The role of fractional crystallization in the genesis of tin-mineralized early syn-D₃ granites (G1–G6) from the Carrazeda de Ansiães area has been previously evidenced by Teixeira et al. (2012b). This mechanism is recurrently invoked to explain the occurrence of Sn-bearing granites in similar geological contexts (Neiva, 1984, 2002; Lehmann, 1990; Gomes and Neiva, 2002; Neiva et al., 2011b; Jiang et al., 2015; Ding et al., 2017; Chen et al., 2018; Feng et al., 2018). The absence of cassiterite in the independent magmatic pulse G7 and in granites of the differentiation series G8–G10 precludes a significant retention of Sn in micas. There is indeed a progressive enrichment in Sn from G8 to G9 and G10, which may be explained by its increase in the hosted biotite and primary muscovite (Fig. 9). This points to a concentration conditioned by a fractional crystallization mechanism, where the low $f\text{O}_2$ favours the enrichment of Sn in residual liquids (Lehmann, 1990; Chicharro et al., 2016;

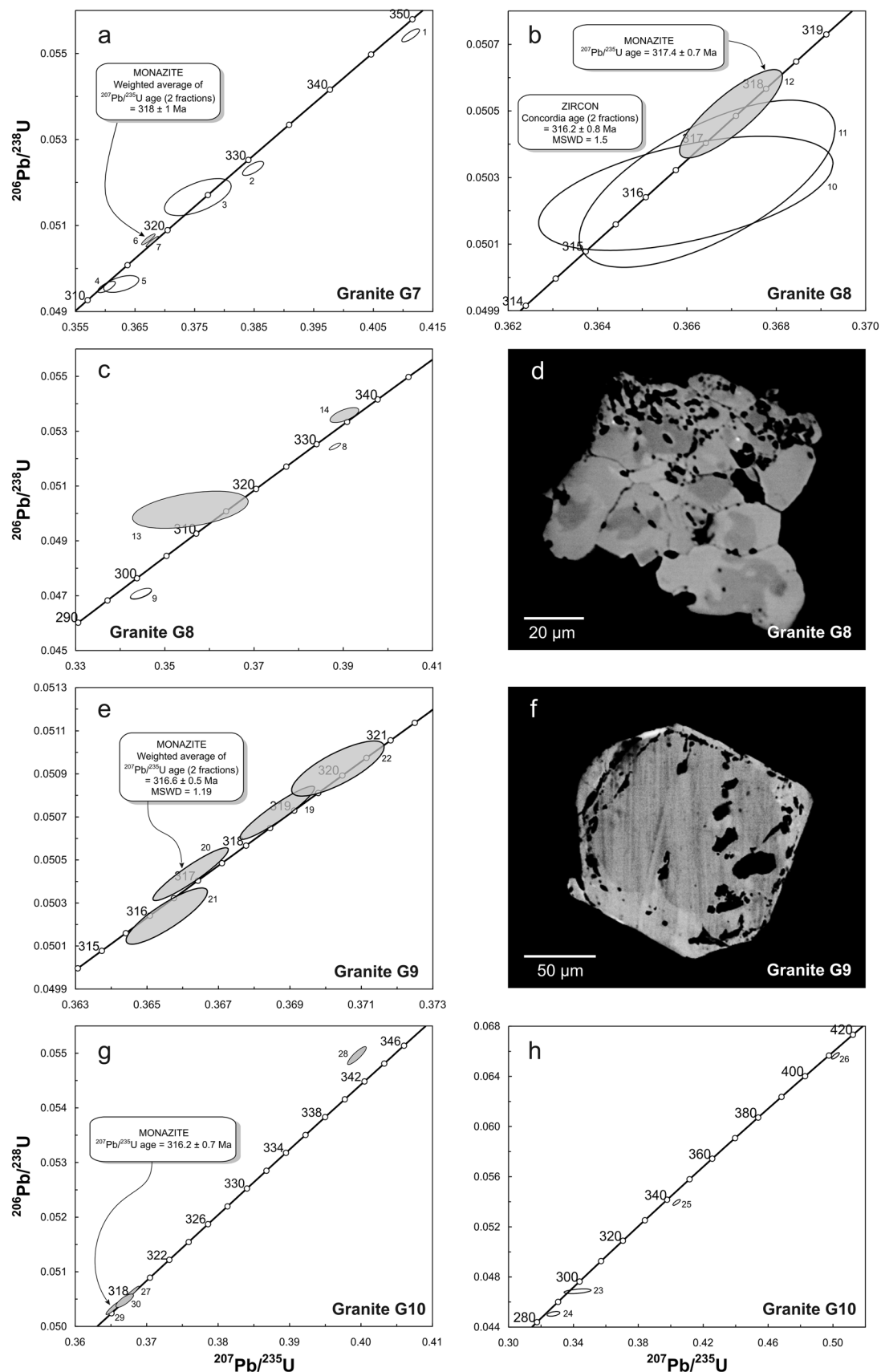


Fig. 6 Concordia diagrams displaying the U–Pb data for zircon (white ellipses) and monazite (gray ellipses) for the four units of the suite, with error ellipses drawn at 2σ , and BSE images of isolated monazite crystals. The resorbed texture of the monazite from granite G8 (**d**) was probably the result of an alteration process, whereas in the subhedral monazite from granite G9 there is evidence of an inherited core (**e**)

Qiu et al., 2017; Roda-Robles et al., 2018; Cao et al., 2020; Cruz et al., 2020). In the log Sn—log Rb/Sr plot (Fig. 10) the correlation line for G8, G9 and G10 follows a Sn enrichment where the fractionation trend is traceable back to below 1 ppm Sn in the least evolved portions, showing that there was no primary Sn enrichment (Lehmann, 1990), in agreement with the low Sn values of the host metasedimentary rocks (< 5 ppm; Teixeira et al., 2012b). Therefore these granites do not reflect a crustal anomaly in Sn.

Despite the similar to marginally lower Sn contents in primary muscovite, when compared to those in the coexisting biotite (Supplemental electronic data Table 4 and Fig. 9), muscovite would retain more Sn than biotite due to its higher abundance in the rock (Table 2). In fact, of the total amount of Sn in the whole rock, primary muscovite would retain an average of 15% in G7, 15% in G8, 15% in G9 and 18% in G10, while biotite would hold an average of 14% in G7, 15% in G8, 10% in G9 and 4% in G10. Therefore, with the increasing degree of differentiation from G7 to G10, the percentage of Sn retained in muscovite tends to increase, while that retained in biotite decreases.

The tin-bearing granites from the Central Iberian Zone are the parent rocks of mineralisations that mainly occur in pegmatites and quartz veins (Neiva, 1984; Lehmann, 1990; Almeida et al., 2002; Neiva and Ramos, 2010), although cassiterite may also occur in some aplites (Charoy and Noronha, 1996), greisens (Wang et al., 2017) and locally in granites (Gomes and Neiva, 2002). In general, these specialized granites result from the partial melting of metasedimentary rocks, as indicated by Sr and Nd isotope data from different areas of Portugal and Spain (Neiva, 2002; Neiva et al., 2009, 2011a; Ruiz et al., 2008), other domains of the Variscan orogenic belt, like the Cornubian batholith, England (Müller et al., 2006) and Erzgebirge, Germany (Romer et al., 2016), and elsewhere, e.g., in the W–Sn polymetallic metallogenic belt at the southeast Yunnan Province in the southwestern Yangtze Block, South China (Liu et al., 2020).

11 Conclusions

This study in northern Portugal concerns a mesozonal granitic suite intruded into Precambrian to Ordovician metasedimentary rocks during the syn-kinematic stages of the Variscan orogeny. This multiphase granitic complex evolved

as ten intrusive phases as identified from field, geochemical and isotopic data.

Granites of Group II (G7–G9) display an internal NW–SE foliation concordant with the regional metasedimentary structures, suggesting that they were affected by the last stages of the third phase of deformation (D_3) of the Variscan orogeny while in the magmatic state. Granite G10 belongs to Group III and is characterized by a strong brittle deformation, probably due to its preferential emplacement in late NNE–SSW fault zones. The U–Pb ages for zircon and monazite show that these granites are the youngest of the Carrazeda de Ansiães area (318 ± 1 Ma to 316.2 ± 0.7 Ma).

Granites G7 and G8 are peraluminous and have similar $(^{87}\text{Sr}/^{86}\text{Sr})_{317}$, ϵNd_{317} and $\delta^{18}\text{O}$ values, but distinct major, trace and rare earth element contents and compositions of feldspars and micas. Granite G8 resulted from a higher degree of partial melting of the same metasedimentary source, probably metapelitic, than granite G7.

Granite G8 magma evolved by fractional crystallization, which is confirmed by the major and trace element trends defined by G8, G9 and G10, the decrease in REE contents from G8 to G10, their similar $(^{87}\text{Sr}/^{86}\text{Sr})_i$, ϵNd_i and $\delta^{18}\text{O}$ values, but also by the compositions of feldspars and micas. Granites G9 and G10 are derived from granite G8 magma by fractionation of quartz, K-feldspar, plagioclase, biotite and ilmenite.

Fractional crystallization increased the Sn content of magma within the G8–G9–G10 series. Tin-bearing granites G7 and G10 do not represent a crustal anomaly of Sn.

The high geothermal gradients due to the middle Carboniferous Variscan continent–continent collision and the subsequent post-thickening extension, probably accompanied by the intrusion of mantle-derived magmas in the lower crust, caused partial melting of crustal material.

Supplementary Information The online version contains supplementary material available at <https://doi.org/10.1007/s41513-020-00160-x>.

Acknowledgements This paper corresponds to a part of the PhD thesis of R. J. S. Teixeira. We are grateful to Prof. Robert Nesbitt who managed the EU SOCFAC facility (HPRI-1999-CT-00108) that led to access to geochemical facilities at the University of Southampton (United Kingdom), Dr. Andy Milton (at the same institution) for the skilled assistance in the laser ablation ICP-MS laboratory, Prof. José Ignacio Gil Ibarguchi, Dr. Sonia García de Madinabeitia and Dr. María Eugenia Sanchez Lorda for the Rb–Sr and Sm–Nd isotopic data obtained at the Geochronology and Isotope Geochemistry- SGILker Facility of the Universidad del País Vasco UPV/EHU (Spain). Prof. Fred J. Longstaffe for the oxygen-isotope analyses obtained at the Department of Earth Sciences, University of Western Ontario (Canada). R. J. S. Teixeira also thanks to Álvaro Miranda, Dr. Alvaro Rubio, Márcio Silva, Miguel Fernández, Nelson Pinto, Simão Botelho and Tito Azevedo for their help in field and laboratory works. Funding was provided to R. J. S. Teixeira by the SFRH/BD/17246/2004 PhD Grant from FCT—Fundação para a Ciência e a Tecnologia, Portugal, and another grant from SOCFAC (Southampton Oceanography Centre, Facilities and Co-Operation). This research was financially supported by the Pole

Table 3 U-Pb data of zircon and monazite from granites G7-G10 of Carraceda de Ansiães area, northern Portugal

Frac-tion characteristics ¹	Mineral	Weight ² (μg)	U^2 (ppm)	Pb^3 (ppm)	Th/U^4	Pb^5 (ppm)	$^{206}\text{Pb}/^{204}\text{Pb}^6$	$^{207}\text{Pb}/^{235}\text{U}^7$	$^{208}\text{Pb}/^{238}\text{U}^7$	ρ^8	$\text{Age}_{^{206}\text{Pb}^*/^{238}\text{U}^7}$ (Ma)	2σ	$\text{Age}_{^{207}\text{Pb}^*/^{235}\text{U}^7}$ (Ma)	2σ	$^{208}\text{Pb}^*/^{206}\text{Pb}^{*7}$ (Ma)	2σ	Disc. ⁹ (%)		
Granite G7 (sample GL23)																			
1	Z eu lp [2]	4.0	754	40	0.11	0.74	2125	0.41127	0.00122	0.05542	0.00012	0.80	347.7	0.8	349.8	0.9	363.6	4.0	4.5
2	Z eu lp [7]	0.5	5638	295	0.22	9.44	1398	0.38481	0.00145	0.05233	0.00013	0.72	328.8	0.8	350.6	1.1	343.1	5.9	4.3
3	Z eu lp in [1]	0.5	1366	84	0.57	8.97	360	0.37555	0.00458	0.05166	0.00035	0.59	324.7	2.2	323.8	3.4	316.9	22.2	-2.5
4	Z eu lp b [18]	1.0	6495	313	0.10	12.50	1416	0.36022	0.00121	0.04957	0.00011	0.72	311.9	0.7	312.4	0.9	316.0	5.3	1.3
5	Z eu lp in [8]	0.5	4190	218	0.15	21.66	528	0.36269	0.00242	0.04964	0.00016	0.51	312.3	1.0	314.2	1.8	328.4	13.0	5.0
6	Mz eu eq y g	11.0	797	186	13.56	0.36	4731	0.36715	0.00091	0.05067	0.00010	0.90	318.6	0.6	317.5	0.7	309.7	2.4	-3.0
7	Mz eu eq y g [7] NA	9.0	2330	414	9.31	0.66	8409	0.36777	0.00085	0.05061	0.00010	0.95	318.3	0.6	318.0	0.6	315.9	1.7	-0.8
Granite G8 (sample QV8)																			
8	Z sb fr y in [8]	3.0	589	42	1.75	0.13	2372	0.36992	0.00134	0.05072	0.00013	0.71	319.0	0.8	319.6	1.0	324.3	5.8	5.8
9	Z eu lp in [4]	0.5	174	10	0.72	0.00	331	0.36856	0.00829	0.05026	0.00023	0.44	316.1	1.4	318.6	6.1	336.6	46.6	46.6
10	Z eu lp y in [1]	0.5	514	27	0.59	0.00	662	0.36331	0.00418	0.04982	0.00017	0.44	313.4	0.9	314.7	3.2	324.1	23.5	23.5
11	Z eu lp y in [3]	0.5	2634	135	0.33	4.28	1009	0.36176	0.00193	0.04972	0.00015	0.63	312.8	0.9	313.5	1.4	318.8	9.4	9.4
12	Z eu lp y in [1]	0.5	894	48	0.36	4.00	363	0.36676	0.00433	0.04928	0.00015	0.46	310.1	1.1	317.2	3.1	370.3	24.0	24.0
13	Z eu lp y in [F]	13.0	571	32	0.60	2.14	789	0.35925	0.00169	0.04922	0.00010	0.51	309.7	0.6	311.7	1.3	326.1	9.2	9.2
14	Mz sb eq y [1]	1.0	199	55	15.81	0.17	315	0.37652	0.00845	0.05182	0.00025	0.42	325.7	1.5	324.5	6.2	315.9	46.7	46.7
NA																			
Granite G9 (sample GC5)																			
15	Z eu sp in [1]	0.5	1929	203	0.89	12.11	659	0.70285	0.00379	0.08511	0.00024	0.55	526.6	1.4	540.5	2.3	599.7	9.7	12.7
16	Z eu sp in [1]	0.5	772	77	0.12	0.00	3123	0.93128	0.00406	0.10585	0.00037	0.72	648.6	2.2	668.3	2.1	735.3	6.4	12.4
17	Z eu sp in [3]	0.5	3334	328	0.45	3.91	2500	0.77825	0.00247	0.09394	0.00024	0.83	578.8	1.4	584.5	1.4	606.6	3.8	4.8
18	Z eu lp in [4]	0.5	615	35	0.36	0.14	541	0.42120	0.00550	0.05649	0.00019	0.47	354.2	1.2	356.9	3.9	374.4	26.5	5.5
19	Mz eu eq y g [2] NA	8.0	1322	182	6.47	0.03	15.200	0.36864	0.00085	0.05072	0.00010	0.93	318.9	0.6	318.6	0.6	316.5	1.9	-0.8
20	Mz eu y g [2] NA	0.5	26.320	2875	4.50	9.49	6202	0.36622	0.00086	0.05043	0.00010	0.93	317.2	0.6	316.8	0.6	314.5	2.0	-0.9
21	Mz eu eq y [2] NA	1.0	5457	1055	10.55	1.93	4384	0.36555	0.00093	0.05024	0.00011	0.86	316.0	0.7	316.4	0.7	319.1	2.9	1.0
22	Mz eu eq y [4] NA	1.0	3353	735	12.03	2.79	2254	0.37033	0.00106	0.05092	0.00011	0.78	320.2	0.6	319.9	0.8	317.7	4.0	-0.8
Granite G10 (sample GA13)																			
23	Z eu lp [1]	1.0	251	13	0.39	1.31	241	0.34255	0.00684	0.04686	0.00015	0.45	295.2	0.9	299.1	5.2	329.7	41.9	10.7
24	Z eu lp [1]	1.0	575	25	0.12	0.90	577	0.32769	0.00326	0.04505	0.00015	0.45	284.1	0.9	287.8	2.5	318.1	20.2	10.9
25	Z eu lp b [4]	4.0	6570	346	0.07	18.13	1218	0.40360	0.00189	0.05394	0.00019	0.80	338.7	1.2	344.3	1.4	382.0	6.3	11.6
26	Z eu lp in [1]	0.5	3075	190	0.12	0.00	3160	0.50153	0.00195	0.06564	0.00021	0.79	409.8	1.3	412.7	1.3	429.1	5.3	4.6
27	Mz sb eq y g [1] NA	8.0	2075	422	11.11	0.19	14.873	0.36783	0.00086	0.05060	0.00010	0.95	318.2	0.6	318.0	0.6	317.0	1.7	-0.4
28	Mz eu eq y g [1] NA	6.0	1044	102	3.40	0.16	7278	0.39926	0.00106	0.05496	0.00013	0.88	344.9	0.8	341.1	0.8	315.3	2.9	-9.6
29	Mz eu eq y [6]	3.0	7206	1182	8.34	3.66	5284	0.36533	0.00089	0.05033	0.00010	0.93	316.5	0.6	316.2	0.7	313.6	2.1	-1.0
NA																			

Table 3 (continued)

Frac-tion Mineral characteristics ¹	Weight ² (μg)	U ² (ppm)	Pb ³ (ppm)	Th/U ⁴ (ppm)	Pbc ⁵ (ppm)	²⁰⁶ Pb/ ²⁰⁴ Pb ⁶	²⁰⁷ Pb/ ²³⁵ U ⁷	2σ (abs) ²⁰⁶ Pb/ ²³⁸ U ⁷	ρ^8	Δ_{age} ²⁰⁶ Pb*/ ²³⁸ U ⁷ (Ma)	2σ (Ma)	Δ_{age} ²⁰⁷ Pb*/ ²³⁵ U ⁷ (Ma)	2σ (Ma)	Disc. ⁹ (%)	
30 Mz en eq y g [6] NA	1.0	4788	768	8.02	4.89	2221	0.36684	0.00100	0.00010	0.81	317.3	0.6	317.3	3.7	0.0

¹Zircon, *Mz* monazite, *eu* euhedral, *sb* subhedral, *eq* equant, *sp* short prismatic (length/width ≈ 2–4), *lp* long prismatic (length/width > 4), *fr* fragment, *b* brown, *y* yellow, *g* green, *in* inclusions, *f/N* number of grains in fraction (*f* > 50 grains); non abraded (all other minerals abraded); unless otherwise specified all the zircons were clear and transparent

^{2,3,5}Weight and concentrations are known to be better than 10%, except for those near and below the ca. 1 μg limit of resolution of the balance

³Total Pb

⁴Th/U model ratio inferred from ²⁰⁸Pb/²⁰⁶Pb ratio and age of sample

⁵Initial common Pb

⁶Raw data corrected for fractionation and blank

⁷Corrected for fractionation, spike, blank and initial common Pb; error calculated by propagating the main sources of uncertainty; initial common Pb corrected using Stacey and Kramers (1975) model Pb

⁸(Rho)—Error correlation factor

⁹Degree of discordancy

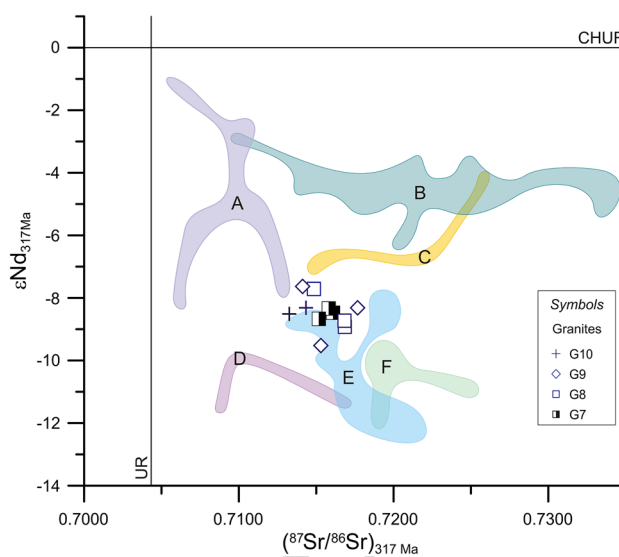


Fig. 7 Diagram of $\varepsilon\text{Nd}_{320\text{ Ma}}$ versus $(^{87}\text{Sr}/^{86}\text{Sr})_{320\text{ Ma}}$ of granites G7–G10 from Carrazeda de Ansiães area, northern Portugal. Results of field projections for **a** felsic peraluminous granulites (lower-crustal xenoliths; Villaseca et al., 1999); **b** metasediments from Beiras Group (Beetsma, 1995; Tassinari et al., 1996) and southern CIZ (Villaseca et al., 2014), **c** orthogneisses from the Spanish Central System (Villaseca et al., 1998), **d** pelitic peraluminous granulites (lower-crustal xenoliths; Villaseca et al., 1999), **e** metasediments from Douro Group (Teixeira et al., 2012a, b) and northern CIZ (Villaseca et al., 1998, 2014) and **f** metasediments from Ordovician units of Central Iberian Zone and Galicia-Trás-os-Montes Zone and from Silurian units of Galicia-Trás-os-Montes (Beetsma, 1995)

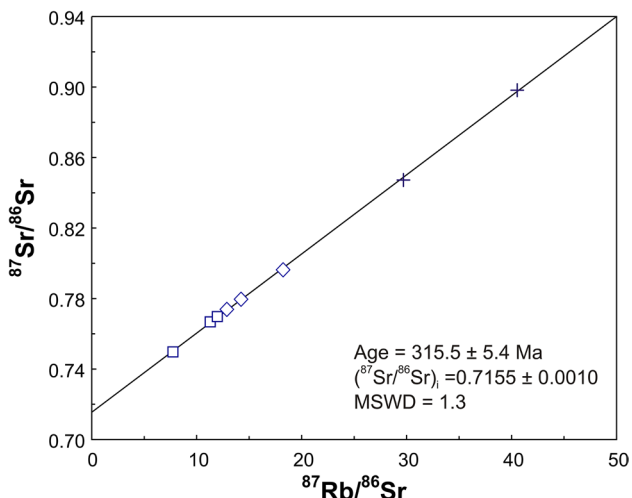


Fig. 8 Whole rock Rb–Sr isochron diagram for granites G8, G9 and G10 from Carrazeda de Ansiães area, northern Portugal

of the Geosciences Centre (CGeo) and projects UIDB/00073/2020 and UIDP/00073/2020 through FCT—Portuguese Foundation for Sciences and Technology. Very helpful constructive reviews and comments were

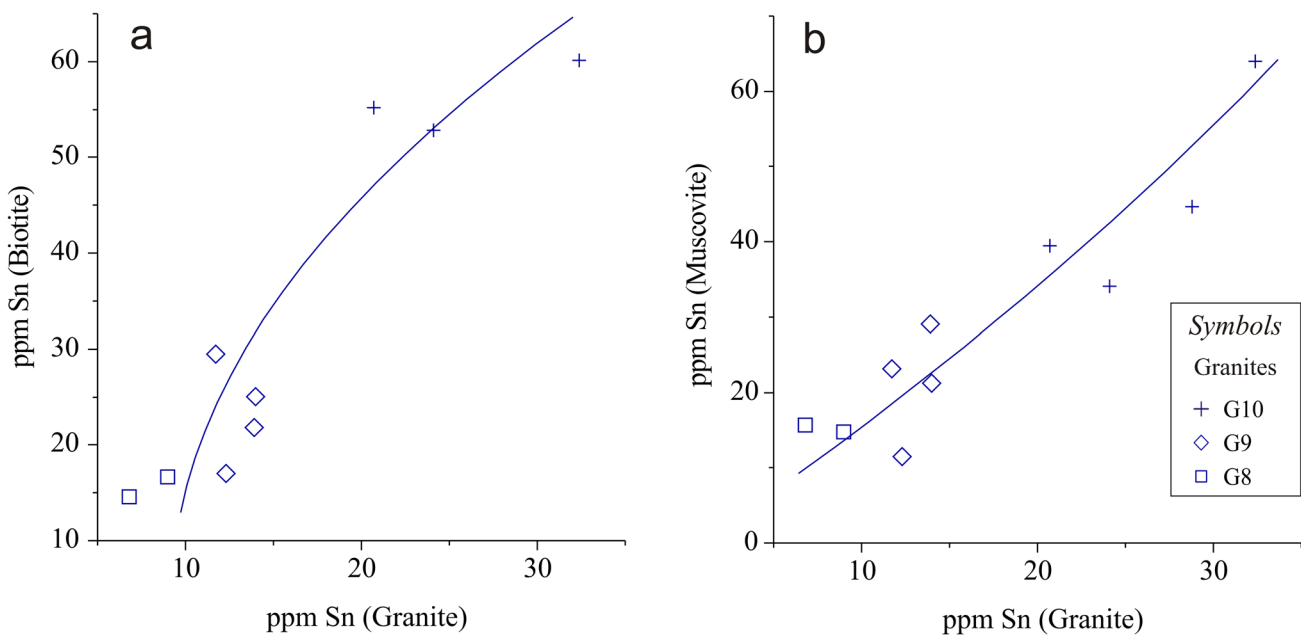


Fig. 9 Plots and trend lines of whole rock Sn versus Sn in: **a** biotite and **b** muscovite of series G8, G9 and G10 from Carrazeda de Ansiães area, northern Portugal

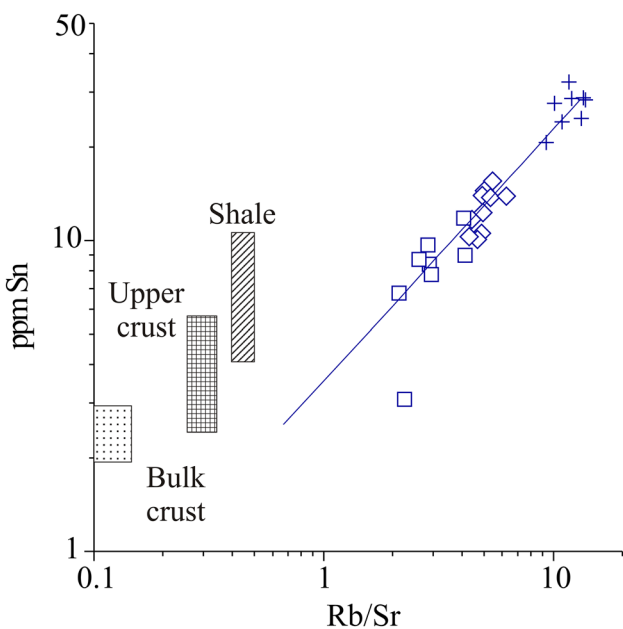


Fig. 10 Correlation of log Rb/Sr—log Sn for series G8, G9 and G10 from Carrazeda de Ansiães area, northern Portugal. Global reference fields from Lehman (1990)

895 provided by two anonymous referees. We are also grateful to the Guest
896 Editors for the final comments.

References

- | | |
|--|--|
| Almeida, M. A., Martins, H. C., & Noronha, F. (2002). Hercynian acid magmatism and related mineralizations in Northern Portugal. <i>Gondwana Research</i> , 5, 423–434.
Antunes, I. M. H. R., Neiva, A. M. R., Silva, M. M. V. G., & Corfu, F. (2008). Geochemistry of S-type granitic rocks from the reversely zoned Castelo Branco pluton (central Portugal). <i>Lithos</i> , 103(3–4), 445–465. https://doi.org/10.1016/j.lithos.2007.10.003 .
Arth, J. G. (1976). Behaviour of trace elements during magmatic processes—a summary of theoretical models and their applications. <i>Journal of Research of the United States Geological Survey</i> , 4, 41–47.
Azevedo, M. R., & Nolan, J. (1998). Hercynian late-post-tectonic granitic rocks from the Fornos de Algodres area (Northern Central Portugal). <i>Lithos</i> , 44(1–2), 1–20. https://doi.org/10.1016/S0024-4937(98)00019-X .
Azevedo, M. R., & Valle Aguado, B. (2006). Origem e instalação de granitóides variscos na Zona Centro-Iberica. In R. Dias, A. Araújo, P. Terrinha, & J. Kullberg (Eds.), <i>Geologia de Portugal no contexto da Ibéria</i> (pp. 107–121). Évora: Universidade de Évora.
Batchelor, R. A., & Bowden, P. (1985). Petrogenetic interpretation of granitoid rock series using multicationic parameters. <i>Chemical Geology</i> , 48, 43–55.
Bea, F. (1996). Residence of REE, Y, Th and U in granites and crustal protoliths; implications for the chemistry of crustal melts. <i>Journal of Petrology</i> , 37(3), 521–552. https://doi.org/10.1093/petrology/37.3.521 .
Bea, F., Montero, P., & Zinger, T. (2003). The nature and origin of the granite source layer of central iberia: evidence from trace element, Sr and Nd isotopes, and zircon age patterns. <i>Journal of Geology</i> , 111, 579–595. | 897
898
899
900
901
902
903
904
905
906
907
908
909
910
911
912
913
914
915
916
917
918
919
920
921
922
923
924
925
926
927
928 |
|--|--|

- Beetsma, J. J. (1995). *The late Proterozoic/Paleozoic and Hercynian crustal evolution of the Iberian Massif, N Portugal*. Unpublished PhD thesis, Vrije Universiteit Amsterdam, 223 p.
- Blattner, P., Abart, R., Adams, C. J., Faure, K., & Hui, L. (2002). Oxygen isotope trends and anomalies in granitoids of the Tibetan plateau. *Journal of Asian Earth Sciences*, 21(3), 241–250.
- Breiter, K. (2012). Nearly contemporaneous evolution of the A- and S-type fractionated granites in the Krušné hory/Erzgebirge Mts Central Europe. *Lithos*, 151, 105–121. <https://doi.org/10.1016/j.lithos.2011.09.022>.
- Bruylants, H., Westhuizen, W. A., & Schoch, A. E. (1983). The estimation of FeO, F, and H_2O^+ by regression in microprobe analysis of natural biotite. *Journal of Trace and Microprobe Techniques*, 1, 399–413.
- Cao, J., Wu, Q., Yang, X., Deng, X., Li, H., Kong, H., & Xi, X. (2020). Geochemical factors revealing the differences between the Xitian and Dengfuxian composite plutons, middle Qin-Hang Belt: implications to the W-Sn mineralization. *Ore Geology Reviews*. <https://doi.org/10.1016/j.oregeorev.2020.103353>.
- Carvalho, P. C. S., Neiva, A. M. R., Silva, M. M. V. G., & Corfu, F. (2012). A unique sequential melting mechanism for the generation of anatetic granitic rocks from the Penafiel area, northern Portugal. *Lithos*, 155, 110–124. <https://doi.org/10.1016/j.lithos.2012.08.019>.
- Chappell, B. W., & White, A. J. R. (1992). I- and S-type granites in the Lachlan Fold Belt. *Transactions of the Royal Society of Edinburgh Earth Sciences*, 83, 1–26.
- Charoy, B., & Noronha, F. (1996). Multistage growth of a rare-element volatile-rich microgranite at Argemela (Portugal). *Journal of Petrology*, 37, 73–94.
- Chen, X., Liang, H., Richards, J. P., Huang, W., Zhang, J., Wu, J., & Sotiriou, P. (2018). Age and granite association of skarn W mineralization at Niutangjie district, South China Block. *Ore Geology Reviews*, 102, 268–283. <https://doi.org/10.1016/j.oregeorev.2018.09.003>.
- Chicharro, E., Boiron, M. C., López-García, J. Á., Barfod, D. N., & Villaseca, C. (2016). Origin, ore forming fluid evolution and timing of the Logrosán Sn-(W) ore deposits (Central Iberian Zone, Spain). *Ore Geology Reviews*, 72, 896–913. <https://doi.org/10.1016/j.oregeorev.2015.09.020>.
- Clayton, R. N., & Mayeda, T. K. (1963). The use of bromine pentafluoride in the extraction of oxygen from oxides and silicates for isotopic analysis. *Geochimica et Cosmochimica Acta*, 27, 43–52.
- Clemens, J. D. (2003). S-type granitic magmas—petrogenetic issues, models and evidence. *Earth-Science Reviews*, 61, 1–18.
- Coke, C. J. M., Teixeira, R. J. S., Gomes, M. E. P., Corfu, F., & Rubio Ordóñez, A. (2011). Early Ordovician volcanism in Eucásia and Mateus areas, Central Iberian Zone, northern Portugal (Goldschmidt Conference Abstract). *Mineralogical Magazine*, 75(3), 685.
- Corfu, F. (2004). U-Pb age, setting and tectonic significance of the anorthosite-mangerite-charnockite-granite suite, Lofoten-Vesteralen, Norway. *Journal of Petrology*, 56, 2081–2097.
- Corfu, F., & Evans, P. M. (2002). Late Paleoproterozoic monazite and titanite U-Pb ages in the Archean Suomujärvi complex, N Finland. *Precambrian Research*, 116, 171–181.
- Costa, M. M., Neiva, A. M. R., Azevedo, M. R., & Corfu, F. (2014). Distinct sources for syntectonic Variscan granitoids: insights from the Aguilar da Beira region, Central Portugal. *Lithos*, 196–197, 83–98. <https://doi.org/10.1016/j.lithos.2014.02.023>.
- Croudace, I. W., & Gilligan, J. (1990). Versatile and accurate trace element determinations in iron-rich and other geological samples using X-ray fluorescence analysis. *X-ray Spectrometry*, 19, 117–123.
- Croudace, I. W., & Thorpe, O. W. (1988). A low dilution, wavelength dispersive X-ray fluorescence procedure for the analysis of archaeological rock artefacts. *Archaeometry*, 30, 227–236.
- Cruz, C., Sant’Ovaia, H., & Noronha, F. (2020). Magnetic mineralogy of variscan granites from northern Portugal: An approach to their petrogenesis and metallogenetic potential. *Geologica Acta*. <https://doi.org/10.1344/GeologicaActa2020.18.5>.
- Davis, D. W., Blackburn, C. E., & Krogh, T. E. (1982). Zircon U-Pb ages from the Wabigoon. Manitou Lakes Region, Wabigoon Subprovince, northwest Ontario. *Canadian Journal of Earth Sciences*, 19, 254–266.
- De Paolo, D. J. (1981). Trace element and isotopic effects of combined wall rock assimilation and fractional crystallization. *Earth and Planetary Science Letters*, 53, 189–202.
- Dias, R., & Coke, C. (2006). O funcionamento dos grandes acidentes crustais no controlo da gênese e instalação das rochas graníticas na Zona Centro Ibérica. In R. Dias, A. Araújo, P. Terrinha, & J. Kullberg (Eds.), *Geologia de Portugal no contexto da Ibéria* (pp. 1231–1234). Évora: Universidade de Évora.
- Dias, G., Leterrier, J., Mendes, A., Simões, P. P., & Bertrand, J. M. (1998). U-Pb zircon and monazite geochronology of post-collisional Hercynian granitoids from the Central Iberian Zone (Northern Portugal). *Lithos*, 45(1–4), 349–369. [https://doi.org/10.1016/S0024-4937\(98\)00039-5](https://doi.org/10.1016/S0024-4937(98)00039-5).
- Dias, G., Simões, P. P., Ferreira, N., & Leterrier, J. (2002). Mantle and crustal sources in genesis of late-Hercynian granitoids (NW Portugal). Geochemical and Sr-Nd isotopic constraints. *Gondwana Research*, 5, 287–305.
- Didier, J., & Barbarin, B. (1991). The different types of enclaves in granites—nomenclature. In J. Didier & B. Barbarin (Eds.), *Enclaves in granite petrology developments in petrology* (Vol. 13, pp. 19–23). Amsterdam: Elsevier.
- Ding, J., Han, C., Xiao, W., Wang, Z., & Song, D. (2017). Geochronology, geochemistry and Sr-Nd isotopes of the granitic rocks associated with tungsten deposits in Beishan district, NW China, Central Asian Orogenic Belt: Petrogenesis, metallogenetic and tectonic implications. *Ore Geology Reviews*, 89, 441–462. <https://doi.org/10.1016/j.oregeorev.2017.06.018>.
- Feng, C., Wang, H., Xiang, X., & Zhang, M. (2018). Late Mesozoic granite-related W-Sn mineralization in the northern Jiangxi region, SE China: a review. *Journal of Geochemical Exploration*, 195, 31–48. <https://doi.org/10.1016/j.gexplo.2018.06.008>.
- Ferreira, N., Iglesias, M., Noronha, F., Pereira, E., Ribeiro, A., & Ribeiro, M. L. (1987). Granitóides da zona Centro-Ibérica e seu enquadramento geodinâmico. In F. Bea, A. Carmina, J. C. Gonzalo, M. L. Plaza, & J. M. L. Rodrigues (Eds.), *Geología de los granitoids y rocas asociadas del Macizo Hespérico, Libro Homenagem a L.C.G. Figueirola* (pp. 37–53). Madrid: Editorial Rueda.
- Förster, H.-J., & Romer, R. L. (2010). Carboniferous magmatism. In U. Linnemann & R. L. Romer (Eds.), *The pre-mesozoic geology of saxo-thuringia—from the cadomian active margin to the variscan orogen* (pp. 287–308). Stuttgart: Schweizerbart Science Publishers.
- Frost, B. R., & Frost, C. D. (2008). A geochemical classification for feldspathic igneous rocks. *Journal of Petrology*, 49(11), 1955–1969. <https://doi.org/10.1093/petrology/egn054>.
- Garcia-Arias, M., & Stevens, G. (2017). Phase equilibrium modelling of granite magma petrogenesis: B. An evaluation of the magma compositions that result from fractional crystallization. *Lithos*, 277, 109–130. <https://doi.org/10.1016/j.lithos.2016.09.027>.
- Gioncada, A., Mazzuoli, R., & Milton, A. J. (2005). Magma mixing at Lipari (Aeolian Islands, Italy): insights from textural and compositional features of phenocrysts. *Journal of Volcanology and Geothermal Research*, 145, 97–118.

- 1059 Gomes, M. E. P., & Neiva, A. M. R. (2002). Petrogenesis of tin-bearing
1060 granites from Ervedosa, northern Portugal: the importance of
1061 magmatic processes. *Chemie Der Erde*, 62(1), 47–72. <https://doi.org/10.1078/0009-2819-00002>.
1062
- 1063 Gomes, M. E. P., Teixeira, R. J. S., Neiva, A. M. R., & Corfu, F. (2014).
1064 Geoquímica e geocronologia dos granitóides da região de Bem-
1065 posta-Picote, Nordeste de Portugal. *Comunicações Geológicas*,
1066 101, 115–118.
1067 Gutiérrez-Alonso, G., Fernández-Suárez, J., López-Carmona, A., &
1068 Gártner, A. (2018). Exhuming a cold case: the early granodiorites
1069 of the northwest Iberian Variscan belt-A Visean magmatic flare-
1070 up? *Lithosphere*, 10(2), 194–216. <https://doi.org/10.1130/L706.1>.
1071 Harris, N. B. W., Pearce, J. A., & Tindle, A. G. (1986). Geochemical
1072 characteristics of collision zone magmatism. In M. P. Coward &
1073 A. C. Ries (Eds.), *Collision tectonics* (pp. 67–81). London: The
1074 Geological Society of London.
1075 Henderson, P. (1984). Chapter 1—general geochemical properties
1076 and abundances of the rare earth elements. In P. B. T.-D. in G.
1077 Henderson (Ed.), *Rare Earth Element Geochemistry* (Vol. 2,
1078 pp. 1–32). Elsevier. <https://doi.org/10.1016/B978-0-444-42148-7.50006-X>
1079 Hoefs, J. (2009). *Stable Isotope Geochemistry* (6th ed.). Berlin Heidelberg: Springer-Verlag.
1080 Hoefs, J., & Emmermann, R. (1983). The oxygen isotopic composition
1081 of Hercynian granites and pre-Hercynian gneisses from the
1082 Schwarzwald, SW Germany. *Contributions to Mineralogy and*
1083 *Petrology*, 83, 320–329.
1084 Holtz, F., & Barbey, P. (1991). Genesis of peraluminous granites II.
1085 Mineralogy and chemistry of the Tourem complex (northern
1086 Portugal). Sequential melting vs. restite unmixing. *Journal of*
1087 *Petrology*, 32, 959–978.
1088 Huang, L.-C., & Jiang, S.-Y. (2014). Highly fractionated S-type granites
1089 from the giant Dahutang tungsten deposit in Jiangnan Orogen,
1090 Southeast China: geochronology, petrogenesis and their
1091 relationship with W-mineralization. *Lithos*, 202–203, 207–226.
1092 <https://doi.org/10.1016/j.lithos.2014.05.030>.
1093 Jaffey, A. H., Flynn, K. F., Glendenin, L. E., Bentley, W. C., & Essling,
1094 A. M. (1971). Precision measurement of half-lives and specific
1095 activities of U235 and U238. *Physical Review C*, 4(5), 1889–
1096 1906. <https://doi.org/10.1103/PhysRevC.4.1889>.
1097 Jiang, S., Peng, N., Huang, L., Xu, Y., Zhan, G., & Dan, X. (2015).
1098 Geological characteristic and ore genesis of the giant tungsten
1099 deposits from the Dahutang ore-concentrated district in northern
1100 Jiangxi Province. *Yanshi Xuebao/Acta Petrologica Sinica*, 31(3),
1101 639–655.
1102 Jung, S., & Pfänder, J. A. (2007). Source composition and melting
1103 temperatures of orogenic granitoids: constraints from CaO/Na₂O,
1104 Al₂O₃/TiO₂ and accessory mineral saturation thermometry. *European Journal of Mineralogy*, 19, 859–870.
1105 Krogh, T. E. (1973). A low contamination method for hydrothermal
1106 decomposition of zircon and extraction of U and Pb for isotopic
1107 age determination. *Geochimica et Cosmochimica Acta*, 37,
1108 485–494.
1109 Krogh, T. E. (1982). Improved accuracy of U-Pb zircon ages by
1110 creation of more concordant systems using an air abrasion technique.
1111 *Geochimica et Cosmochimica Acta*, 46, 637–649.
1112 La Roche, H., Letterier, J., Grand Claude, P., & Marchal, M. (1980).
1113 A classification of volcanic and plutonic rocks using R₁–R₂ dia-
1114 grams and major elements analyses—its relationships with cur-
1115 rent nomenclature. *Chemical Geology*, 29, 183–210.
1116 Le Maitre, R., Streckeisen, A., Zanettin, B., Le Bas, M., Bonin, B.,
1117 & Bateman, P. (Eds.). (2002). *Igneous Rocks: A Classification*
1118 *and Glossary of Terms: Recommendations of the International*
1119 *Union of Geological Sciences Subcommission on the Systematics*
1120 *of Igneous Rocks* (2nd ed.). Cambridge: Cambridge University
1121 Press. <https://doi.org/10.1017/CBO9780511535581>
- 1122 Ledru, P., Courrioux, G., Dallain, C., Lardeaux, J.-M., Montel, J.-M.,
1123 Vanderhaeghe, O., & Vitel, G. (2001). The Velay dome (French
1124 Massif Central): melt generation and granite emplacement during
1125 orogenic evolution. *Tectonophysics*, 342, 207–227.
1126 Lehmann, B. (1990). *Metallogenesis of tin. Lecture Notes in Earth Sci-*
1127 *ences*. Berlin: Springer-Verlag.
1128 Li, C., Yan, J., Yang, C., Song, C.-Z., Wang, A.-G., & Zhang, D.-Y.
1129 (2020). Generation of leucogranites via fractional crystallization:
1130 a case study of the Jurassic Bengbu granite in the southeast-
1131 ern North China Craton. *Lithos*. <https://doi.org/10.1016/j.lithos.2019.105271>.
1132 Liew, T. C., & Hofmann, A. W. (1988). Precambrian crustal compo-
1133 nents, plutonic associations, plate environment of the Hercynian
1134 Fold Belt of Central Europe: indications from a Nd and Sr study.
1135 *Contributions to Mineralogy and Petrology*, 98, 129–138.
1136 Liu, Y., Zhang, L., Mo, X., Santosh, M., Dong, G., & Zhou, H. (2020).
1137 The giant tin polymetallic mineralization in southwest China:
1138 integrated geochemical and isotopic constraints and implications
1139 for Cretaceous tectonomagmatic event. *Geoscience Frontiers*.
1140 <https://doi.org/10.1016/j.gsf.2020.01.007>.
1141 London, D., Černý, P., Loomis, J. L., & Pan, J. L. (1990). Phosphorus
1142 in alkali feldspars of rare-element granitic pegmatites. *American*
1143 *Mineralogist*, 28, 771–786.
1144 London, D., Wolf, M. B., Morgan, G. B., & Garrido, M. G. (1999).
1145 Experimental silicate-phosphate equilibria in peraluminous granitic
1146 magmas, with a case study of the Alburquerque batholith at Tres Arroyos,
1147 Badajoz Spain. *Journal of Petrology*, 40(1), 215–240. <https://doi.org/10.1093/petroj/40.1.215>.
1148 Ludwig, K. R. (1999). Isoplot/Ex version 2.03. *A geochronological*
1149 *toolkit for Microsoft Excel*. Berkeley Geochronology under Spe-
1150 cial Publication, 1, 43 pp.
1151 Martins, H. C. B., Sant'Ovaia, H., & Noronha, F. (2009). Genesis and
1152 emplacement of felsic Variscan plutons within a deep crustal
1153 lineation, the Penacova-Régua-Verín fault: an integrated geo-
1154 physics and geochemical study (NW Iberian Peninsula). *Lithos*,
1155 111, 142–155.
1156 Martins, H. C. B., Sant'Ovaia, H., & Noronha, F. (2013). Late-Variscan
1157 emplacement and genesis of the Vieira do Minho composite plu-
1158 ton, Central Iberian Zone: constraints from U-Pb zircon geochro-
1159 nology, AMS data and Sr-Nd-O isotope geochemistry. *Lithos*,
1160 162–163, 221–235. <https://doi.org/10.1016/j.lithos.2013.01.001>.
1161 Merino Martínez, E., Villaseca, C., Orejana, D., Pérez-Soba, C., Belou-
1162 sova, E., & Andersen, T. (2014). Tracing magma sources of three
1163 different S-type peraluminous granitoid series by in situ U-Pb
1164 geochronology and Hf isotope zircon composition: the Variscan
1165 Montes de Toledo batholith (central Spain). *Lithos*, 200–201(1),
1166 273–298. <https://doi.org/10.1016/j.lithos.2014.04.013>.
1167 Miller, C. F., Hanchar, J. M., Wooden, J. L., Bennett, V. C., Harrison,
1168 T. M., Wark, D. A., & Foster, D. A. (1992). Source region of
1169 a granite batholiths: evidence from lower crustal xenoliths and
1170 inherited accessory minerals. *Transactions of the Royal Society*
1171 *of Edinburgh: Earth Sciences*, 83, 49–62.
1172 Miller, C. F., McDowell, S., & Mapes, R. W. (2003). Hot and cold
1173 granites? Implications of zircon saturation temperatures and
1174 preservation of inheritance. *Geology*, 31, 529–532.
1175 Miller, C. F., Stoddard, E. F., Bradfish, L. J., & Dollase, W. A. (1981).
1176 Composition of plutonic muscovite: genetic implications. *Canadian*
1177 *Mineralogist*, 19(1), 25–34.
1178 Monier, G., Mergoil-Daniel, J., & Labernardiére, H. (1984). Généra-
1179 tions successives de muscovites et feldspaths potassiques dans les
1180 leucogranites du massif de Millevaches (Massif Central français).
1181 *Bulletin de Minéralogie*, 107(1), 55–68. <https://doi.org/10.3406/bulmi.1984.7793>.
1182 Müller, A., Seltmann, R., Halls, C., Siebel, W., Dulski, P., Jeffries, T.,
1183 et al. (2006). The magmatic evolution of the Land's End pluton,
1184

- 1190 Cornwall, and associated pre-enrichment of metals. *Ore Geology*
1191 *Reviews*, 28, 329–367.
- 1192 Nachit, H., Razafimahafa, N., Stussi, J. M., & Carron, J. P. (1985).
1193 Composition chimique des biotites et typologie magmatique des
1194 granitoïdes. *Comptes Rendus de l'Académie Des Sciences, Paris,*
1195 *Serie II*, 301(11), 813–818.
- 1196 Nash, W. P., & Crecraft, H. R. (1985). Partition coefficients for trace
1197 elements in silicic magmas. *Geochimica et Cosmochimica Acta*,
1198 49(11), 2309–2322. [https://doi.org/10.1016/0016-7037\(85\)90231-5](https://doi.org/10.1016/0016-7037(85)90231-5).
- 1199 Neiva, A. M. R. (1984). Geochemistry of tin-bearing granitic
1200 rocks. *Chemical Geology*, 43(3–4), 241–256. [https://doi.org/10.1016/0009-2541\(84\)90052-4](https://doi.org/10.1016/0009-2541(84)90052-4).
- 1201 Neiva, A. M. R. (1994). Dating and geochemistry of tin-bearing
1202 granitic rocks and their minerals from NE of Gerez mountain,
1203 Northern Portugal. *Boletín de la Sociedad Española de Minerología*, 17, 65–82.
- 1204 Neiva, A. M. R. (1998). Geochemistry of highly peraluminous granites
1205 and their minerals between Douro and Tamega valleys, northern
1206 Portugal. *Chemie der Erde*, 58, 161–184.
- 1207 Neiva, A. M. R. (2002). Portuguese granites associated with Sn-W
1208 and Au mineralizations. *Bulletin of the Geological Society of
1209 Finland*, 74, 79–101.
- 1210 Neiva, A. M. R., & Gomes, M. E. P. (2001). Diferentes tipos de
1211 granitos e seus processos petrogenéticos: granitos hercínicos por-
1212 tuguenses. *Memórias da Academia das Ciências de Lisboa*, 31,
1213 53–95.
- 1214 Neiva, A. M. R., & Ramos, J. M. F. (2010). Geochemistry of granite
1215 aplite-pegmatite sills and petrogenetic links with granites,
1216 Guarda-Belmonte area, central Portugal. *European Journal of
1217 Mineralogy*, 22(6), 837–854.
- 1218 Neiva, A. M. R., Silva, P. B., Corfu, F., & Ramos, J. M. F. (2011a).
1219 Sequential melting and fractional crystallization: granites from
1220 Guarda-Sabugal area, central Portugal. *Geochemistry*, 71(3),
1221 227–245. <https://doi.org/10.1016/j.chemer.2011.06.002>.
- 1222 Neiva, A. M. R., Silva, P. B., & Ramos, J. M. F. (2011b). Geochemis-
1223 try of granitic aplite-pegmatite veins and sills and their miner-
1224 als from the Sabugal area, central Portugal. *Neues Jahrbuch für
1225 Mineralogie*, 189(1), 49–74.
- 1226 Neiva, A. M. R., Williams, I. S., Ramos, J. M. F., Gomes, M. E. P.,
1227 Silva, M. M. V. G., & Antunes, I. M. H. R. (2009). Geochemical
1228 and isotopic constraints on the petrogenesis of Early Ordovician
1229 granodiorite and Variscan two-mica granites from the Gouveia
1230 area, central Portugal. *Lithos*, 111(3–4), 186–202. <https://doi.org/10.1016/j.lithos.2009.01.005>.
- 1231 Nekvasil, H. (1992). Ternary feldspar crystallization in high-tempera-
1232 ture felsic magmas. *American Mineralogist*, 77, 592–604.
- 1233 Nguyen, T. A., Yang, X., Thi, H. V., Liu, L., & Lee, I. (2019). Piaoac
1234 granites related W-Sn mineralization, northern Vietnam: evi-
1235 dences from geochemistry, zircon geochronology and Hf iso-
1236 topes. *Journal of Earth Science*, 30(1), 52–69. <https://doi.org/10.1007/s12583-018-0865-6>.
- 1237 Oliveira, J., Pereira, E., Piçarra, J., Young, T., & Romano, M. (1992).
1238 O Paleozóico Inferior de Portugal: síntese da estratigrafia e da
1239 evolução paleogeográfica. In J. C. Gutiérrez Marco, J. Saavedra,
1240 & I. Rábano (Eds.), *Paleozóico Inferior de Ibero-América* (pp.
1241 359–375). Badajoz: Universidad de Extremadura.
- 1242 Otamendi, J. E., Nullo, F. E., Patiño Douce, A. E., & Fagiano, M.
1243 (1998). Geology, mineralogy and geochemistry of syn-orogenic
1244 anatexic granites from the Achiras Complex, Córdoba, Argen-
1245 tina: some petrogenetic and geodynamic implications. *Journal
1246 of South American Earth Sciences*, 11(4), 407–423.
- 1247 Pan, X., Hou, Z., Zhao, M., Chen, G., Rao, J., Li, Y., et al. (2018).
1248 Geochronology and geochemistry of the granites from the Zhuxi
1249 W-Cu ore deposit in South China: implication for petrogenesis,
1250 geodynamical setting and mineralization. *Lithos*, 304–307, 155–
1251 179. <https://doi.org/10.1016/j.lithos.2018.01.014>.
- 1252 Pearce, J. A., Harris, N. B. W., & Tindle, A. G. (1984). Trace element
1253 discrimination diagrams for the tectonic interpretation of granitic
1254 rocks. *Journal of Petrology*, 25, 956–983.
- 1255 Pereira, M. F., Castro, A., Fernández, C., & Rodríguez, C. (2018).
1256 Multiple Paleozoic magmatic-orogenic events in the Central
1257 Extremadura batholith (Iberian Variscan belt, Spain). *Journal
1258 of Iberian Geology*, 44(2), 309–333. <https://doi.org/10.1007/s41513-018-0063-5>.
- 1259 Pin, C., & Santos Zalduogui, J. F. (1997). Sequential separation of
1260 light rare-earth elements, thorium and uranium by miniaturized
1261 extraction chromatography: application to isotopic analyses of
1262 silicate rocks. *Analytica Chimica Acta*, 339(1–2), 79–89. [https://doi.org/10.1016/S0003-2670\(96\)00499-0](https://doi.org/10.1016/S0003-2670(96)00499-0).
- 1263 Poitrasson, F., Chenery, S., & Bland, D. J. (1996). Contrasted mona-
1264 zite hydrothermal alteration mechanisms and their geochemical
1265 implications. *Earth and Planetary Science Letters*, 145(1–4),
1266 79–96. [https://doi.org/10.1016/s0012-821x\(96\)00193-8](https://doi.org/10.1016/s0012-821x(96)00193-8).
- 1267 Qiu, Z., Yan, Q., Li, S., Wang, H., Tong, L., Zhang, R., et al. (2017).
1268 Highly fractionated Early Cretaceous I-type granites and related
1269 Sn polymetallic mineralization in the Jinkeng deposit, eastern
1270 Guangdong, SE China: constraints from geochronology, geo-
1271 chemistry, and Hf isotopes. *Ore Geology Reviews*, 88, 718–738.
1272 <https://doi.org/10.1016/j.oregeorev.2016.10.008>.
- 1273 Rieder, M., Cavazzini, G., D'Yakonov, Y. S., Frank-Kamenetskii, V.
1274 A., Gottardi, G., Guggenheim, S., et al. (1998). Nomenclature of
1275 the micas. *Canadian Mineralogist*, 36(3), 905–912. <https://doi.org/10.1180/minmag.1999.063.2.13>.
- 1276 Roda-Robles, E., Villaseca, C., Pesquera, A., Gil-Crespo, P. P., Vieira,
1277 R., Lima, A., & Garate-Olave, I. (2018). Petrogenetic relation-
1278 ships between Variscan granitoids and Li-(F-P)-rich aplite-peg-
1279 matites in the Central Iberian Zone: geological and geochemical
1280 constraints and implications for other regions from the Euro-
1281 pean Variscides. *Ore Geology Reviews*, 95, 408–430. <https://doi.org/10.1016/j.oregeorev.2018.02.027>.
- 1282 Romer, R. L., Förster, H.-J., & Hahne, K. (2012). Strontium isotopes—
1283 a persistent tracer for the recycling of Gondwana crust in the
1284 Variscan orogen. *Gondwana Research*, 22(1), 262–278. <https://doi.org/10.1016/j.gr.2011.09.005>.
- 1285 Romer, R. L., & Kroner, U. (2016). Phanerozoic tin and tungsten min-
1286 eralization-Tectonic controls on the distribution of enriched pro-
1287 tooliths and heat sources for crustal melting. *Gondwana Research*,
1288 31, 60–95. <https://doi.org/10.1016/j.gr.2015.11.002>.
- 1289 Ruiz, C., Fernández-Leyva, C., & Locutura, J. (2008). Geochemistry,
1290 geochronology and mineralisation potential of the granites in the
1291 Central Iberian Zone: the Jalama batholith. *Chemie Der Erde*,
1292 68(4), 413–429. <https://doi.org/10.1016/j.chemer.2006.11.001>.
- 1293 Schärer, U. (1984). The effect of initial ^{230}Th disequilibrium on young
1294 U-Pb ages: the Makalu case Himalaya. *Earth and Planetary
1295 Science Letters*, 67(2), 191–204. [https://doi.org/10.1016/0012-821X\(84\)90114-6](https://doi.org/10.1016/0012-821X(84)90114-6).
- 1296 Silva, A. F., Rebelo, J. A., & Ribeiro, M. L. (1989). *Notícia explicativa
1297 da Folha 11-C (Torre de Moncorvo)*. Lisboa: Serviços Geológi-
1298 cos de Portugal.
- 1299 Silva, A. F., Rebelo, J. A., Santos, A.J., Cardoso, F., Ribeiro, M.L.,
1300 Ribeiro, A., Cabral, J. & Estagiários da F.C.L. (1987/88). Carta
1301 Geológica de Portugal à escala 1:50 000 (Folha 11-C, Torre de
1302 Moncorvo). Serviços Geológicos de Portugal
- 1303 Simons, B., Andersen, J. C. Ø., Shail, R. K., & Jenner, F. E. (2017).
1304 Fractionation of Li, Be, Ga, Nb, Ta, In, Sn, Sb, W and Bi in the
1305 peraluminous Early Permian Variscan granites of the Cornubian
1306 Batholith: Precursor processes to magmatic-hydrothermal min-
1307 eralisation. *Lithos*, 278–281, 491–512. <https://doi.org/10.1016/j.lithos.2017.02.007>.

- 1320 Simons, B., Shail, R. K., & Andersen, J. C. O. (2016). The petrogenesis
1321 of the Early Permian Variscan granites of the Cornubian Batholith:
1322 Lower plate post-collisional peraluminous magmatism in
1323 the Rhenohercynian Zone of SW England. *Lithos*, 260, 76–94.
1324 <https://doi.org/10.1016/j.lithos.2016.05.010>.
- 1325 Smith, W. D., Darling, J. R., Bullen, D. S., Lasalle, S., Pereira, I.,
1326 Moreira, H., et al. (2019). Zircon perspectives on the age and
1327 origin of evolved S-type granites from the Cornubian Batholith,
1328 Southwest England. *Lithos*, 336–337, 14–26. <https://doi.org/10.1016/j.lithos.2019.03.025>.
- 1329 Sousa, L. (2000). *Estudo da fracturação e das características físico-
1330 mecânicas de granitos da região de Trás-os-Montes com vista à
1331 sua utilização como rocha ornamental*. Unpublished PhD thesis,
1332 University of Trás-os-Montes e Alto Douro, 479 p.
- 1333 Stacey, J. S., & Kramers, J. D. (1975). Approximation of terrestrial lead
1334 isotope evolution by a two-stage model. *Earth and Planetary
1335 Science Letters*, 26(2), 207–221. [https://doi.org/10.1016/0012-821X\(75\)90088-6](https://doi.org/10.1016/0012-
1336 821X(75)90088-6).
- 1337 Steiger, R. H., & Jäger, E. (1977). Subcommission on geochronology:
1338 convention on the use of decay constants in geo- and cosmochemistry.
1339 *Earth and Planetary Science Letters*, 36(3), 359–362.
1340 [https://doi.org/10.1012-821X\(77\)90060-7](https://doi.org/10.1016/0012-821X(77)90060-7).
- 1341 Sylvester, A. G. (1998). Magma mixing, structure, and re-evaluation of
1342 the emplacement mechanism of Vrådal pluton, central Telemark,
1343 southern Norway. *Norsk Geologisk Tidskrift*, 78, 259–276.
- 1344 Tassinari, C. C. G., Medina, J., & Pinto, M. S. (1995). Rb-Sr and
1345 Sm-Nd geochronology and isotope geochemistry of Central Iberian
1346 metasedimentary rocks (Portugal). *Geologie en Mijnbouw*,
1347 75, 69–79.
- 1348 Taylor, S. R., & McLennan, S. M. (1985). *The continental crust: its
1349 composition and evolution*. Carlton: Blackwell Scientific
1350 Publication.
- 1351 Teixeira, R. J. S. (2008). *Mineralogia, petrologia e geoquímica dos
1352 granitos e seus encraves da região de Carrazeda de Ansiães*.
1353 Unpublished PhD thesis, University of Trás-os-Montes e Alto
1354 Douro, 430 p.
- 1355 Teixeira, R. J. S., Neiva, A. M. R., Gomes, M. E. P., Corfu, F., Cuesta,
1356 A., & Croudace, I. W. (2012a). The role of fractional crystallization
1357 in the genesis of early syn-D 3, tin-mineralized Variscan
1358 two-mica granites from the Carrazeda de Ansiães area, northern
1359 Portugal. *Lithos*, 153, 177–191. <https://doi.org/10.1016/j.lithos.2012.04.024>.
- 1360 Teixeira, R. J. S., Coke, C., Dias, R., & Gomes, M. E. P. (2012b). U-Pb
1361 geochronology of detrital zircons from a metaconglomerate of
1362 the Formation of São Domingos (Group of Douro), Desejosa/
1363 Castanheiro do Sul, Northern Portugal. *European Mineralogical
1364 Conference*, 1, 442.
- 1365 Teixeira, R. J. S., Coke, C., Gomes, M. E. P. & Corfu, F. (2013a). ID-
1366 TIMS U-Pb ages of Tremadocian-Floian ash-fall tuff beds from
1367 Marão and Eucíssia areas, Northern Portugal. *William Smith
1368 Meeting 2013: The First Century of Isotope Geochronology: the
1369 Legacy of Frederick Soddy & Arthur Holmes – Abstract Book*,
1370 152–154.
- 1371 Teixeira, R. J. S., Coke, C., Gomes, M. E. P., Dias, R., & Martins, L.
1372 O. (2013b). U-Pb geochronology of detrital zircons from meta-
1373 sedimentary rocks from Formation of Desejosa, Serra do Marão,
1374 Portugal. (Goldschmidt Conference Abstract). *Mineralogical
1375 Magazine*, 77(5), 2318.
- 1376 Teixeira, R. J. S., Neiva, A. M. R., Silva, P. B., Gomes, M. E. P.,
1377 Andersen, T., & Ramos, J. M. F. (2011). Combined U-Pb geo-
1378 chronology and Lu-Hf isotope systematics by LAM-ICPMS of
1379 zircons from granites and metasedimentary rocks of Carrazeda
1380 de Ansiães and Sabugal areas, Portugal, to constrain granite
1381 sources. *Lithos*, 125(1–2), 321–334. <https://doi.org/10.1016/j.lithos.2011.02.015>.
- 1382 Teixeira, R. J. S., Urbano, E. E. M. C., Gomes, M. E. P., Meireles, C.,
1383 Corfu, F., Santos, J. F., et al. (2015). Interbedded quartz-muscovite
1384 layers in the ferriferous quartzites of the Lower Ordovician
1385 deposits of Moncorvo synclinorium (NE Portugal): an example
1386 of volcanogenic metasedimentary deposits? *Comunicações
1387 Geológicas*, 102(Special Is), 31–39.
- 1388 Tischendorf, G., Gottesmann, B., Foster, H.-J., & Trumbull, R. B.
1389 (1997). On Li-bearing micas: estimating Li from electron micro-
1390 probe analyses and an improved diagram for graphical represen-
1391 tation. *Mineralogical Magazine*, 61, 809–834.
- 1392 Valle Aguado, B., Azevedo, M. R., Schaltegger, U., Martínez Catalán,
1393 J. R., & Nolan, J. (2005). U-Pb zircon and monazite geochronol-
1394 ogy of Variscan magmatism related to syn-convergence exten-
1395 sion in Central Northern Portugal. *Lithos*, 82(1–2 SPEC. ISS.),
1396 169–184. <https://doi.org/10.1016/j.lithos.2004.12.012>.
- 1397 Villaseca, C., Barbero, L., & Rogers, G. (1998). Crustal origin of Her-
1398 cynian peraluminous granitic batholiths of Central Spain: petro-
1399 logical, geochemical and isotopic (Sr, Nd) constraints. *Lithos*,
1400 43, 55–79.
- 1401 Villaseca, C., Downes, H., Pin, C., & Barbero, L. (1999). Nature and
1402 composition of the lower continental crust in central spain and
1403 the granulite-granite linkage: inferences from Granulitic Xeno-
1404 liths. *Journal of Petrology*, 40(10), 1465–1496.
- 1405 Villaseca, C., Merino, E., Oyarzun, R., Orejana, D., Pérez-Soba, C., &
1406 Chicharro, E. (2014). Contrasting chemical and isotopic signa-
1407 tures from Neoproterozoic metasedimentary rocks in the Central
1408 Iberian Zone (Spain) of pre-Variscan Europe: implications for
1409 terrane analysis and Early Ordovician magmatic belts. *Precam-
1410 brian Research*, 245, 131–145. <https://doi.org/10.1016/j.precamres.2014.02.006>.
- 1411 Villaseca, C., Pérez-Soba, C., Merino, E., Orejana, D., López-García,
1412 J. A., & Billstrom, K. (2008). Contrasting crustal sources for per-
1413 aluminous granites of the segmented Montes de Toledo Batho-
1414 lith (Iberian Variscan Belt). *Journal of Geosciences*, 53(3–4),
1415 263–280. <https://doi.org/10.3190/jgeosci.035>.
- 1416 Wang, F., Bagas, L., Jiang, S., & Liu, Y. (2017). Geological, geo-
1417 chemical, and geochronological characteristics of Weilasituo Sn-
1418 poly-metallic deposit, Inner Mongolia, China. *Ore Geology Reviews*,
1419 80, 1206–1229. <https://doi.org/10.1016/j.oregeorev.2016.09.021>.
- 1420 Wang, L.-X., Ma, C.-Q., Zhang, C., Zhang, J.-Y., & Marks, M. A. W.
1421 (2014). Genesis of leucogranite by prolonged fractional crystal-
1422 lization: a case study of the Mufushan complex South China.
1423 *Lithos*, 206–207(1), 147–163. <https://doi.org/10.1016/j.lithos.2014.07.026>.
- 1424 Wasserburg, G. J., Jacobsen, S. B., De Paolo, D. J., McCulloch, M. T.,
1425 & Wen, T. (1981). Precise determination of Sm/Nd ratios, Sm
1426 and Nd isotopic abundances in standard solutions. *Geochimica
1427 et Cosmochimica Acta*, 45, 2311–2323.
- 1428 Watson, E. B., & Harrison, T. M. (1983). Zircon saturation revis-
1429 ited: temperature and composition effects in a variety of crustal
1430 magma types. *Earth and Planetary Science Letters*, 64, 295–304.
- 1431 Williamson, B. J., Shaw, A., Downes, H., & Thrillwall, M. F. (1996).
1432 Chemical constraints on the genesis of Hercynian two-mica
1433 leucogranites from the Massif Central. *Chemical Geology*, 127,
1434 25–42.
- 1435 Xu, B., Jiang, S.-Y., Wang, R., Ma, L., Zhao, K.-D., & Yan, X. (2015).
1436 Late Cretaceous granites from the giant Dulong Sn-polymetallic
1437 ore district in Yunnan Province, South China: geochronology,
1438 geochemistry, mineral chemistry and Nd-Hf isotopic composi-
1439 tions. *Lithos*, 218–219, 54–72. <https://doi.org/10.1016/j.lithos.2015.01.004>.
- 1440 Yurimoto, H., Duke, E. F., Papike, J. J., & Shearer, C. K. (1990). Are
1441 discontinuous chondrite-normalized REE patterns in pegmatitic
1442 granitic systems the results of monazite fractionation? *Geochim-
1443 ica et Cosmochimica Acta*, 54, 2141–2145.
- 1444

1450 Zhang, L.-X., Wang, Q., Zhu, D.-C., Li, S.-M., Zhao, Z.-D., Zhang,
1451 L.-L., et al. (2019). Generation of leucogranites via fractional
1452 crystallization: a case from the Late Triassic Luoza batholith

in the Lhasa Terrane, southern Tibet. *Gondwana Research*, 66,
63–76. <https://doi.org/10.1016/j.gr.2018.08.008>.

1453

1454

REVISED PROOF